

Characterization of three-dimensional vortical structures in the wake past a circular cylinder in the transitional regime ^{EP}

Cite as: Phys. Fluids **32**, 074104 (2020); <https://doi.org/10.1063/5.0011311>

Submitted: 21 April 2020 . Accepted: 17 June 2020 . Published Online: 07 July 2020

Wasim Sarwar , and Fernando Mellibovsky 

COLLECTIONS

 This paper was selected as an Editor's Pick



View Online



Export Citation



CrossMark

ARTICLES YOU MAY BE INTERESTED IN

[Effects of external magnetic fields on the rheology and magnetization of dilute emulsions of ferrofluid droplets in shear flows](#)

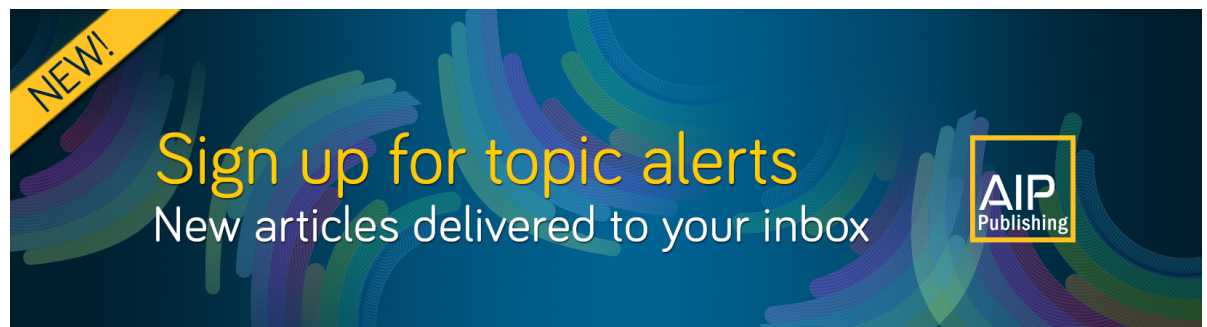
Physics of Fluids **32**, 073306 (2020); <https://doi.org/10.1063/5.0009983>

[Three-dimensional wake dynamics behind a tapered cylinder with large taper ratio](#)

Physics of Fluids **32**, 063604 (2020); <https://doi.org/10.1063/5.0010960>

[Acoustic-wave-induced cooling in onset of hypersonic turbulence](#)

Physics of Fluids **32**, 061702 (2020); <https://doi.org/10.1063/5.0011871>



NEW!

Sign up for topic alerts
New articles delivered to your inbox



Characterization of three-dimensional vortical structures in the wake past a circular cylinder in the transitional regime

Cite as: Phys. Fluids 32, 074104 (2020); doi: 10.1063/5.0011311

Submitted: 21 April 2020 • Accepted: 17 June 2020 •

Published Online: 7 July 2020



View Online



Export Citation



CrossMark

Wasim Sarwar  and Fernando Mellibovsky ^{a)} 

AFFILIATIONS

Department of Physics, Aerospace Engineering Division, Universitat Politècnica de Catalunya, 08034 Barcelona, Spain

^{a)} Author to whom correspondence should be addressed: fernando.mellibovsky@upc.edu

ABSTRACT

The flow past a circular cylinder in the transitional regime at $Re = 2000$ has been thoroughly investigated via well resolved direct numerical simulation with a spectral element code. Spanwise periodic boundary conditions of at least $L_z \geq 2.5D$ are required to properly reproduce first and second order turbulent statistics in the cylinder wake. A Kelvin–Helmholtz instability can already be detected at this relatively low Reynolds number at the flapping shear layers issued from either side of the cylinder. The instability, with a frequency $f_{KH} \approx 0.84$ that is in excellent agreement with published experimental results, arises only occasionally and the associated spanwise vortices are subject to spanwise localization. We show that while Kármán vortices remain predominantly two-dimensional, streamwise vortical structures appearing along the braids connecting consecutive vortices are mainly responsible for rendering the flow three-dimensional. These structures may appear in isolation or in vortex pairs and have a typical spanwise wavelength of around $\lambda_z \approx 0.20$ – 0.28 at a location at $(x, y) = (3, 0.5)$, as measured via Hilbert transform along probe arrays with spanwise orientation. In line with experimental and numerical results at higher $Re = 3900$, the size of the structures drops in the very near-wake to a minimum at $x \approx 2.5$ and then steadily grows to asymptotically attain a finite maximum for $x \geq 20$. A time-evolution-based stability analysis of the underlying two-dimensional vortex shedding flow, which happens to be chaotic, shows that the fastest growing perturbations in the linear regime have a spanwise periodicity $\lambda_z \approx 0.3$ and are located in the very near-wake, right within the braid that connects the last forming Kármán vortex with the previous one, thus hinting at a close relation with the fully developed vortical structures observed in full-fledged three-dimensional computations.

Published under license by AIP Publishing. <https://doi.org/10.1063/5.0011311>

I. INTRODUCTION

The incompressible viscous flow around a circular cylinder constitutes a canonical problem for the study of separated flow past bluff bodies.¹ A wealth of experimental and numerical studies have been conducted on this geometry over many decades, covering a wide range of flow regimes,² so as to analyze a variety of flow phenomena including laminar and turbulent boundary layer separation,^{3,4} detached shear layer and wake instabilities,⁵ or vortex shedding.⁶

The steady symmetric wake behind the cylinder destabilizes supercritically at $Re \gtrsim 47$ ($Re = UD/\nu$ is the Reynolds number based on cylinder diameter D , upstream flow velocity U , and fluid kinematic viscosity ν) into a periodic space-time-symmetric flow

regime named after von Kármán and characterized by alternate shedding of counter-rotating vortices from either side of the cylinder.^{7,8} This unsteady regime and further transitions retaining some of its features are a source of mean aerodynamic drag increase,^{9,10} fluid–structure resonant interaction,^{11,12} structural vibration,¹³ and acoustic noise.^{14,15}

The periodic two-dimensional vortex-shedding state has been observed to persist up to $Re \lesssim 190$, beyond which point three-dimensionality sets in.¹⁶ Two distinct three-dimensional modes have been reported in the range $Re \in [180, 260]$ in the so-called wake-transition regime, namely, mode A and mode B. Mode A is characterized by the onset of vortex loops that are stretched by shear into streamwise vortex pairs with a spanwise wavelength of around 3 to $4D$. Observation of mode A has been reported from as low as

$Re \gtrsim 180$ such that it coexists with two-dimensional vortex shedding within a small Re -range, the flow behavior being hysteretical and, accordingly, the spanwise-invariance-breaking bifurcation being slightly subcritical.¹⁷ Mode B occurs at a slightly higher $Re \gtrsim 250$ with the characteristic wavelength in the order of $1D$ ¹⁸ and is related to a second spanwise-invariance-breaking bifurcation of the already unstable two-dimensional periodic vortex-shedding state that occurs at $Re \sim 259$.¹⁰ The transition from mode A to mode B involves intermittency (the flow dynamics keeps switching between the two modes) and a gradual transfer of the time-fraction of occurrence of A and B from the former to the latter. At $Re \simeq 260$, mode B is already the dominant structure and exhibits remarkable spanwise coherence. Besides the remarkably different spanwise wavelength, the two modes possess also distinct symmetries that tell them apart (which points at unrelated triggering instability mechanisms) and their inception is responsible for discontinuous leaps in vortex shedding frequency and characteristic slope discontinuities in the dependence of the base pressure coefficient with Re .¹⁶

On top of the small-scale structure of modes A and B, the wake transition regime also involves vortex local phase-dislocations or defects that result in intermittent large-scale spot-like structures that dominate the wake as they are advected downstream.^{19,20} These structures are responsible for low frequency irregular fluctuations in the wake²¹ and a discontinuous drop of vortex shedding frequency.

The shear layers resulting from boundary layer separation at either side of the cylinder are subject to turbulent transition at sufficiently high Re .²² This transition follows a Kelvin–Helmholtz instability that is essentially two-dimensional and only becomes noticeable from $Re \gtrsim 1200$.^{20,23} The resulting vortices accumulate downstream and are subdued into the von Kármán vortices that dominate the cylinder wake.²⁴ Based on outer velocity and boundary layer thickness at separation, a rough estimate predicts that the Kelvin–Helmholtz instability frequency must scale as $f_{KH}/f_{vK} \sim Re^{1/2}$,²⁰ where the subindices in f_{KH} and f_{vK} stand for Kelvin–Helmholtz and von Kármán, respectively. A best fit to a collection of existing experimental data,^{20,25–27} together with physical arguments as to the dependence of shear layer velocity and length scales on Re , suggests that the scaling should rather follow $f_{KH}/f_{vK} \sim Re^{0.67}$.^{23,28}

The shear layers in the cylinder wake remain fairly planar only within a finite extent that is limited by the inception of the wake instability and the onset of von Kármán vortices. As a result, the Kelvin–Helmholtz instability only becomes measurable at Re sufficiently high for the vortices to reach a sufficient amplification within the limited extent for their spatial development, which can be estimated to happen for $Re \gtrsim 1200$.²⁹ The instability, however, must be at play from much lower Re , and the frequency scaling suggests that a resonance with the von Kármán instability is to be expected at $Re \simeq 260$.²³ As a matter of fact, this resonance has been put forward as a plausible argument for the high spanwise coherence that wake structures possess at precisely this value of Re .

It is a well established fact that both the aspect ratio and spanwise boundary conditions have an impact on the vortex shedding past a circular cylinder.^{30,31} A systematic analysis of spanwise correlations in the three dimensional near-wake behind the cylinder reveals that structures with considerable dispersion of spanwise

wavelengths in the range $\lambda_z \in [3, 5]D$ occur in the early wake transition regime,^{24,32–35} dominated by mode A, in accordance with linear stability analyses.^{17,36} The dispersion is significantly reduced when data involving dislocation are systematically discarded so that filtered measurements follow closely the maximum growth-rate mode predicted by Floquet analysis, starting at $\lambda_z^A = 3.96D$ at onset. In the late transition regime, where mode B becomes dominant, the dispersion is much lower and wavelengths $\lambda_z \simeq 1D$ are observed in the near-wake ($x/D < 3$), close enough to the second linear instability of the already unstable two dimensional vortex shedding flow, with $\lambda_z^B = 0.82D$. The vortical structure spanwise size scaling in this region can be estimated as decreasing with $1/\sqrt{Re}$,²⁴ which is confirmed by experiments in the range $Re \in [300–2200]$.³³ In the far wake ($x/D > 10$), however, the same experiments report that the spanwise wavelength becomes fairly independent of Re and remains of order $\lambda_z/D \sim O(1)$.³³

The variation of the spanwise wavelength of streamwise vortices along the wake at fixed Re has been analyzed both experimentally,^{33,37} using both flow visualization and two-probe cross correlation, and numerically,³⁸ through the use of the Hilbert transform. The crossflow sampling location has a large impact on the near-wake structure length scale, which renders any comparison impractical. Sufficiently far downstream away from the cylinder, in the far wake, this effect is less noticeable and the typical wavelength is observed to clearly saturate at a fairly constant value.

There exists ample experimental evidence, backed by sound theoretical arguments, that turbulence in spatially developing flows depends, even asymptotically, on upstream conditions (i.e., the particulars of the turbulent flow generator).^{39,40} This holds true for planar wakes⁴¹ and, in particular, for the turbulent wake past a cylinder. Planar wakes past blunt bodies of characteristic blockage size D can be split in four distinct regions, namely, the near wake ($x/D \lesssim 4$), the mid-wake ($4 \lesssim x/D \lesssim 50$), the far wake ($50 \lesssim x/D \lesssim 1000$), and the asymptotic wake ($x/D \gtrsim 1000$).⁴² The near wake is subject to direct interaction with the wake generator and bears strong correlation with aerodynamic parameters such as the base pressure coefficient or the aerodynamic forces on the body. Beyond this wake formation region, which contains the mean recirculation bubble, no action or perturbation has any measurable effect whatsoever on the flow field around the body. The mid-wake is different from the far wake in that shed vortices remain detectable, while the mean flow becomes self-similar in the far wake. A certain universality develops in the asymptotic wake, if only for conveniently scaled (with the local centerline velocity deficit and the local length scale) mean velocity profiles. Meanwhile, spreading rates and higher order turbulent moments, including Reynolds stresses, can, in principle, depend on upstream conditions.⁴⁰ In the case of the cylinder wake, complete self-preservation has been established experimentally at $Re = 2000$ beyond $x/D \gtrsim 260$.⁴³

While mean flow statistics are fairly independent of Re in the far wake behind a cylinder once within the shear-layer transition regime ($Re \gtrsim 1200$), second order flow statistics (Reynolds stresses) only become so for $Re \gtrsim 10\,000$.⁴⁴

There is considerable consensus as to the mid-wake flow topology within the early shear-layer transition regime, as evidenced by the good agreement across a wide range of experimental^{45–49} and numerical^{49–56} studies of crossflow distribution of mean velocity components at varying flow rates. Higher order flow statistics also

show reasonable agreement provided that sufficiently close Re are considered.

In the near wake, besides the fact that statistics are no longer expected to be independent of Re , results are at odds among the various experimental and numerical studies, even at coincident Re . In trying to shed light on the cause for disagreement, the flow at $Re = 3900$ has become a recurrent benchmark case since the experiments of Lourenco and Shih⁴⁵ and Ong and Wallace.⁴⁷ Two distinct flow states have been reported, named U- and V-type after the outline of the mean streamwise velocity crossflow profile in the very near-wake of the cylinder at $x/D = 1$. The U-state is characterized by a longer recirculation bubble L_r (not to be confused with wake formation length); a slightly higher vortex shedding frequency f_{vK} ; a lower base pressure suction coefficient $-C_{pb} = 2(p_\infty - p_b)/(\rho U_\infty^2)$; lower aerodynamic forces (mean drag C_D and root-mean-square of lift $C_{L_{rms}} = \sqrt{\langle C_L^2 \rangle}$); lower Reynolds stresses $\langle u'u' \rangle$, $\langle u'v' \rangle$, and $\langle v'v' \rangle$; and characteristic double-peak distributions of $\langle u'u' \rangle$ both in the streamwise direction along the wake centerline and in the near-wake cross-stream direction.^{49-51,53-56,62-64} The V-state, in contrast, features a smaller L_r ; slightly lower f_{vK} ; higher $-C_{pb}$, C_D , $C_{L_{rms}}$, and $\langle u'u' \rangle$, $\langle u'v' \rangle$ and $\langle v'v' \rangle$; and inflection plus single-peak streamwise and four-peak cross-stream distributions of $\langle u'u' \rangle$.^{45,53,54,56,62-65} Table I summarizes a number of experiments, along with relevant

experimental conditions and a bunch of flow parameter results that allow characterization of the corresponding type of solution. The experiments, run at several $Re \sim O(10^3)$ on experimental setups of different spanwise extent, include Particle Image Velocimetry (PIV), Laser Doppler Velocimetry (LDV), and Hot Wire Anemometry (HWA) measurements, and varying levels of free-stream turbulence (Tu). Statistics have been collected over variable counts of vortex shedding cycles. It becomes clear from the flow parameter values that V-type solutions are favored at large Re or in the presence of higher Tu , U-type profiles being ubiquitous for sufficiently low Re and low Tu experiments. These studies also seem to point at a gradual transition from one state to the other as Re is increased in the same experimental setup with all other parameters kept constant.

Table II contains an extensive list of numerical simulations of the flow past a circular cylinder at Reynolds numbers relevant to the regime under scrutiny. Summarized alongside the main results (to be compared with the experimental results of Table I) are the most significant simulation parameters such as the numerical method used, the spanwise periodic extent of the domain, the in-plane and spanwise resolutions (and order of the discretization), and the number of vortex shedding cycles collected for statistics. The in-plane domain size and the time discretization method and order

TABLE I. Literature review of experimental results for the flow past a circular cylinder. Reported are, when available, the flow measurement method (HWA: hot wire anemometry; PIV: particle image velocimetry; LDV: laser Doppler velocimetry), preturbulence level Tu , Reynolds number Re , cylinder span size L_z , number of vortex shedding cycles recorded for statistics N_s , von Kármán frequency f_{vK} , Kelvin–Helmholtz frequency f_{KH} , wake instability frequency f_w , recirculation bubble length L_r , mean drag coefficient C_D and rms fluctuation C'_D , lift coefficient rms fluctuation C'_L , base pressure coefficient $-C_{pb}$, and location of the boundary layer separation θ_{sep} .

Author (references)	Method	Tu (%)	Re	Experimental											
				L_z	N_s	f_{vK}	f_{KH}	f_w	L_r	C_D	C'_D	C'_L	$-C_{pb}$	θ_{sep}	
Norberg ²⁷	HWA	0.1	2 000	240	?	0.213									
		0.1	3 000	80		0.213		1.65	0.98			0.84			
		1.4	3 000	80		0.209		1.44	1.03			0.89			
		0.1	8 000	80		0.204		0.99	1.13			1.05			
		1.4	8 000	80		0.199		0.90	1.20			1.12			
Lourenco and Shih ⁴⁵	PIV	?	3 900	21	29				1.18	0.98				85 ± 2	
Ong and Wallace ⁴⁷	HWA	0.67	3 900	84	7680	0.21									
Norberg ⁴⁸	LDV	<0.1	1 500	65	1350				1.79						
		<0.1	3 000	65					1.66						
		<0.1	5 000	65					1.40						
		<0.1	8 000	65					1.17						
		<0.1	10 000	65					1.02						
Norberg ⁵⁷	LDV	<0.1	1 500	105	?	0.212						0.045			
		<0.1	4 400	105		0.210						0.100			
Konstantinidis <i>et al.</i> ⁵⁸	LDV	3.3	1 550	10	?										
		3.3	2 150	10		0.215		1.77							
		3.3	2 750	10											
		3.3	7 450	10											
Konstantinidis <i>et al.</i> ⁵⁹	PIV	3.3	2 160	10	?										
Konstantinidis and Balabani ⁶⁰	PIV	3	2 150	10	?	0.215		1.58							
Dong <i>et al.</i> ⁶¹	PIV	?	4 000	8.78	?			1.47							
Parnaudeau <i>et al.</i> ⁴⁹	PIV	<0.2	3 900	20	250			1.51							
	HWA	<0.2	3 900	20	2856	0.208									

TABLE II. Literature review of numerical results for the flow past a circular cylinder. Besides some of the parameters reported in Table I, listed are the numerical method employed (DNS: direct numerical simulation; LES: Large Eddy simulation; FVM: Finite Volume Method; FDM: Finite Difference Method; SEM: Spectral Element Method; SDM: Spectral Difference Method), the spanwise periodic extent of the domain L_z , the in-plane N_{xy} and spanwise N_z resolutions (the superindex indicates discretization order, F for Fourier), and near wake solution topology Sol (U: U-state; V: V-state; UV: mixed; ?: inconclusive).

Author (references)	Method	Re	Numerical											Sol.				
			L_z	N_z	N_{xy}	N_s	f_{vK}	f_{KH}	f_w	L_r	C_D	$-C_{p_b}$	θ_{sep}					
Present results: Case 1	DNS SEM	2000	1.5	64	$4\,040^8$	66	0.218	1.237		1.50	1.015	0.88	92.0	U				
			Case 2	2	64	$4\,040^8$	58	0.212	1.121		1.58	0.987	0.83	90.3	U			
			Case 3	2.5	128	$5\,484^8$	55	0.215	0.839		1.66	0.975	0.80	90.0	U			
			Case 4	π	96	$5\,484^8$	22	0.211			1.71	0.961	0.79	90.0	U			
Lehmkuhl <i>et al.</i> ⁵⁶	DNS FVM	3900	π	128	72 700	858	0.215	1.34	0.0064	1.36	1.015	0.935	88	UV				
						L:250	0.218		1.55	0.979	0.877	87.8	U					
						H:250	0.214		1.26	1.043	0.98	88.3	V					
						330	0.214		1.363	1.019	0.933		UV					
Gsell <i>et al.</i> ³⁸	DNS FVM	3900	10	300	150 000	3–4	0.21	1.365			0.92		86.8					
												1.35	1.04	0.93	88	UV		
Kravchenko and Moin ⁵⁴	LES FDM	3900	π	48^F	$27\,780^S$	7	0.21											
Ma <i>et al.</i> ⁵³	DNS SEM	3900	$\pi/2$	24	$27\,780$?	0.219											
$(c_s = 0.032)$	LES SEM		1.5π	64^F	902^8		0.213											
$(c_s = 0.196)$	LES SEM		1.5π	64^F	902^8		0.208											
Mittal ⁶⁶	LES FDM	3900	π	48	39 900	7	~ 0.21				1.1	1.15	88	U?				
Mittal ⁵¹	LES FDM	3900	π	48^F	48 120	12				1.40	1.0	0.93	86.9	UV?				
Breuer ⁵²	LES FVM	3900	π	64	27 225	>22	0.215	~ 0.007	1.372	1.016	0.941	87.4	UV					
									0.215	1.043	1.097	1.069	88.5	V				
									0.215	1.686	0.969	0.867	86.7	U				
									0.215	1.115	1.099	1.049	87.9	V				
									0.215	1.114	1.089	1.036	87.9	V				
Franke and Frank ⁵⁵	LES FVM	3900	π	33	35 584	42	0.209		1.64	0.978	0.85	88.2	U					
Dong <i>et al.</i> ⁶¹	DNS SEM	3900	π	128^F	902^8	40–50	0.21?	1.539	1.36				UV					
Chen <i>et al.</i> ⁶⁴	iLES FVM	2580	π	56	70 000	50	0.22		1.66	0.95	0.73		U					
Mohammad <i>et al.</i> ⁶⁷	iLES SDM	2580	π	18^3	$11\,144^3$	20	0.22		1.13	1.03	0.88		V					
Lodato and Jameson ⁶⁸	iLES SDM	2580	3.2	10^3	$1\,847^3$	300							U					
Lodato and Jameson ⁶⁹	DNS FVM	3300	4	512	416 556	10	0.214						87.3	U				
Beaudan and Moin ⁵⁰	DNS FDM	3900	π	256	63 336		0.216						90.3	V				
Tremblay ⁶⁵	DNS FDM	3900	π	8	1024	416 556	0.216						87.4	U				
Tremblay ⁶⁵	DNS FVM	3900	π	48 ⁵	$19\,584^5$	6	0.216		1.56	0.96	0.89	85.3	U					
Tremblay ⁶⁵	DNS FVM	3900	π	112	419 364	60	0.22		1.3	1.03	0.93	85.7	UV					

have been deemed appropriate for all cases and are therefore not reported. In the case of large eddy simulations (LESs), the model and/or subgrid-scale dissipation parameter c_s are also reported. The last column indicates whether the reported results feature a U-type or V-type cross-stream velocity profile in the near wake and/or the statistically averaged results are compatible with one or the other. UV indicates results that appear to be halfway between U- and V-type states, while the question mark denotes inconclusive results.

There has been much controversy as to whether there naturally exists a unique near wake topology or if both states may occur, under what circumstances should one or the other be expected.

Based on L_r and C_{pb} as indirect indicators, a gradual transition from the U-state toward the V-state with the increase in Re has been reported by several experimental studies.^{27,70–72} The U-state would seem to dominate at $Re \sim 2000$, while the V-state has completely taken over from $Re \gtrsim 10000$. This trend has been later confirmed by direct measurement of mean and second order flow statistics in the near wake of the cylinder.⁴⁸ Increased pre-turbulence levels Tu have been shown to shift the gradual transition to slightly lower Re -values,²⁷ while an insufficient cylinder aspect ratio L_z/D , such that the spanwise boundary conditions drive the flow, has a stabilizing effect for the U-state.³¹ This suggests that the spanwise size of near-wake structures might be playing an important role in near-wake flow statistics as numerics seem to substantiate.^{53,61,69} Simulations are usually undertaken with periodic boundary conditions in the spanwise direction, and an insufficient spanwise domain size ($L_z/D \leq \pi$ at $Re = 3900$) has been shown to favor the U-state, with all other parameters kept constant. The V-state can however be artificially recovered in small domains when the spanwise direction is under-resolved^{51,52,54,62,63,66} allegedly due to insufficient viscous dissipation of turbulent kinetic energy. The same applies to overly coarse in-plane resolutions, which also result in V-state selection.^{54,64} In the case of LES simulation, over-dissipative subgrid scale models also tend to induce the U-state even in domains of allegedly sufficient spanwise extent,^{53,64} while under-dissipative models induce V-type profiles in short spanwise domains.^{62–64}

The large scatter of results, which yield conflicting values for most of the mean integral quantities, has occasionally been ascribed to unconverged statistics due to exceedingly short time series of data (insufficient sample size),^{55,62} although this alone cannot explain all of the observed discrepancies. A statistical analysis of near wake velocity time series from direct numerical simulation, spanning over 800 vortex shedding cycles, detected a very low frequency of about 3 of the Strouhal number that was traced back to an instability of the mean recirculation bubble size.⁵⁶ Conditional and phase averaging revealed that the mean statistics might be in fact the weighted mean of two modes, a high and a low energy mode, corresponding to the V-state and U-state, respectively. In this light, the scatter of inconsistent results would be a consequence of averaging too short time series at different phases along the low frequency cycle. The low-pass filtered signals do not consist of memoryless intermittent switching between the two so-called modes such that the scenario of two strange saddles linked by heteroclinic connections can be discarded altogether. The temporal dynamics would rather correspond to an instability of a unique state, although further inquiry shall be required to test this hypothesis. In any case, the

physical mechanism underlying the low frequency evolution of the near wake remains unaccounted for. The loopback mechanism by which the high energy short recirculation bubble should progress toward a lower energy longer bubble and then back remains a mystery. Even though the unconverged statistics issue might apply to almost all preceding numerical studies and a few of the experiments,⁴⁵ most experimental studies analyze sufficiently long data series that the low frequency could have been detected and the mean state obtained.^{27,48,49,58,61} Instead, U-type near wake statistics are reported in most cases.

All things considered, it would seem that there is in fact a gradual shift from U- to V-type near wake statistics as Re is increased and that the former is still dominant at $Re = 3900$. Observation of V-type short recirculation bubbles would therefore be an artifact of either biased statistics or, in the case of numerical simulation, too coarse a resolution to capture the dissipative length scales.

We shall focus here on the cylinder shear layers and wake regime at $Re = 2000$, with the intention of probing the occurrence of the U- and V-states when the Kelvin–Helmholtz instability is perceptible but sufficiently weak that turbulent statistics are modest in the near wake. The reason for this choice of Reynolds number is threefold. To begin with, the experiments by Norberg provide the most accurate experimental results at the lowest Re at which the shear layer instability has been consistently reported. It was our intention to get as far down from $Re = 3900$ as possible to avoid the low frequency wake oscillation reported by Lehmkuhl *et al.*⁵⁶ but still guarantee the detection of the shear layer instability. Finally, the stability analysis of the underlying two-dimensional chaotic flow to three-dimensional perturbations could not be pushed much further beyond $Re = 2000$, as pseudo-modal growth becomes so fast that the methods used become unsuitable. Procuring the fastest-growing three-dimensional pseudo-modes for comparison with fully resolved computational results requires that Re be kept sufficiently low. Comparison with $Re = 3900$ will be established once the simulation has been calibrated against experimental^{23,27,48,57–59,73} and numerical^{64,67–69} data at $Re \in [1500–3000] \sim 2000$, with the objective of gaining some insight on the effects of Reynolds numbers on near-wake turbulent statistics in the early transitional flow past the cylinder.

The outline of the manuscript is as follows. The mathematical formulation is presented in Sec. II alongside the numerical approach undertaken to solve the equations. Section III reports the numerical results in terms of global quantities first, followed by near- and mid-wake turbulent statistics. The instability of the shear layers that flap in the near-wake is investigated in Sec. IV, together with the characterization, in terms of location and spanwise size, of the vortical structures that are responsible for the three-dimensionality of the cylinder wake. The stability analysis of the underlying two-dimensional flow is also undertaken in order to determine the nature of the fastest growing perturbations for comparison against the vortical structures observed in full three-dimensional simulations. Finally, the main findings are summarized in Sec. V.

II. PROBLEM FORMULATION AND NUMERICAL APPROACH

The incompressible flow around an infinitely long spanwise-aligned circular cylinder is governed by the Navier–Stokes

equations, which, after suitable nondimensionalization with cylinder diameter D and upstream flow velocity U , read as

$$\frac{\partial \mathbf{u}}{\partial t} + (\mathbf{u} \cdot \nabla) \mathbf{u} = -\nabla p + \frac{1}{Re} \nabla^2 \mathbf{u}, \quad (1)$$

$$\nabla \cdot \mathbf{u} = 0,$$

where $\mathbf{u}(\mathbf{r}; t) = (u, v, w)$ and $p(\mathbf{r}; t)$ are the nondimensional velocity and pressure, respectively, at nondimensional location $\mathbf{r} = (x, y, z)$ and advective time t . x (u), y (v), and z (w) denote the streamwise, crossflow, and spanwise coordinates (velocity components), respectively. $Re = UD/\nu$ is the Reynolds number. The domain in the streamwise-crossflow plane takes $(x, y) \in [-20, 50] \times [-20, 20]$ (see Fig. 1), while periodic boundary conditions $[\mathbf{u}, p](\mathbf{r} + L_z \hat{\mathbf{k}}; t) = [\mathbf{u}, p](\mathbf{r}; t)$ are assumed in the spanwise direction with periodicity length $L_z = 1.5, 2, 2.5$ and π . The spanwise domain extent has been chosen to fit a minimum of three typical spanwise structures (streamwise vortex pairs) in the near wake, as estimated by the empirical scaling $\lambda_z \sim 20Re^{-0.5}$ at $x = 3$.³³ The size of the structures is known to grow along the wake^{33,47} but not as much as to not fit in the computational domain. The boundary conditions for velocity are unitary Dirichlet at the upstream boundary $\mathbf{u}(-20, y, z) = \hat{\mathbf{i}}$, non-slip on the cylinder wall $\mathbf{u}_w = 0$, slip wall on the upper and lower boundaries $\partial_y u(x, \pm 20, z) = v(x, \pm 20, z) = \partial_y w(x, \pm 20, z) = 0$, and homogeneous Neumann at the downstream boundary $(\nabla \cdot \hat{\mathbf{n}})(50, y, z) = 0$. For pressure, high-order homogeneous Neumann boundary conditions are applied everywhere except for the downstream boundary, where homogeneous Dirichlet conditions $p(50, y, z) = 0$ are imposed. The high-order pressure Neumann boundary conditions are designed consistent for the splitting scheme used in the time-discretization.⁷⁴ Convective-type boundary conditions were considered for the downstream boundary, but as they slowed down the computations while producing no measurable impact on the cylinder wake dynamics, they were discarded altogether on account of the sufficient streamwise extent of the downstream domain.

The flow has been evolved in time using the incompressible Navier–Stokes solver of the tensor-product-based spectral/finite element package Nektar++.⁷⁴ Spatial discretizations of $K = 4040$ and 5484 high-order quadrilateral elements have been employed in the

streamwise-crossflow plane, with Lagrange polynomial expansions up to order $P - 1 = 7$. A continuous Galerkin projection has been enforced across element boundaries. A particularly refined mesh has been set up in the vicinity of the cylinder, as shown in the inset of Fig. 1, to properly resolve boundary layers and separation, as well as in the near wake, where turbulent fluctuations may have significant impact on the flow field topology around the cylinder. Fourier expansions with resolutions ranging from $N_z = \pm 64$ to ± 128 modes have been deployed in the periodic spanwise direction along with Orszag’s 3/2 rule for dealiasing. In order for the discrete operators to preserve the symmetries of their continuous counterparts, the advection term has been written in skew-symmetric form. For the time discretization, a second order velocity-correction splitting scheme with a time step $\Delta t = 0.0002$ has been adopted as providing sufficient time-integration accuracy. Larger time steps might have sufficed accuracy-wise, but the discrete operators resulting from the second order implicit–explicit (IMEX) splitting-scheme employed are stiff and trigger numerical instability for Δt beyond that used. Fully implicit time-discretization schemes might be used with much larger time steps at the cost of having to solve extremely large nonlinear systems of equations at every time step, which renders the time evolution extremely slow and, in our case, unfeasible from a memory storage requirement perspective.

The instantaneous velocity field has been split following

$$\mathbf{u}(\mathbf{r}; t) = \bar{\mathbf{u}}(\mathbf{r}_2) + \underbrace{\mathbf{u}'_2(\mathbf{r}_2; t) + \mathbf{u}_3(\mathbf{r}; t)}_{\mathbf{u}'(\mathbf{r}; t)}, \quad (2)$$

where $\mathbf{r}_2 = (x, y)$ and $\bar{\mathbf{u}} = (\bar{u}, \bar{v}) = \langle \mathbf{u} \rangle_{zt}$ is the spanwise- and time-averaged two-dimensional mean velocity field. $\mathbf{u}' = (u', v', w')$ is the time-dependent (fluctuating) velocity field. The von Kármán spanwise vortex shedding mode is represented by

$$\mathbf{u}'_2(\mathbf{r}_2; t) = \mathbf{u}_2(\mathbf{r}_2; t) - \bar{\mathbf{u}}(\mathbf{r}_2), \quad (3)$$

with $\mathbf{u}_2(\mathbf{r}_2; t) = \langle \mathbf{u} \rangle_z$ as the spanwise-averaged instantaneous two-dimensional velocity field. Finally, $\mathbf{u}_3 = \mathbf{u} - \mathbf{u}_2$ represents the purely three-dimensional perturbation velocity field. The Reynolds stress

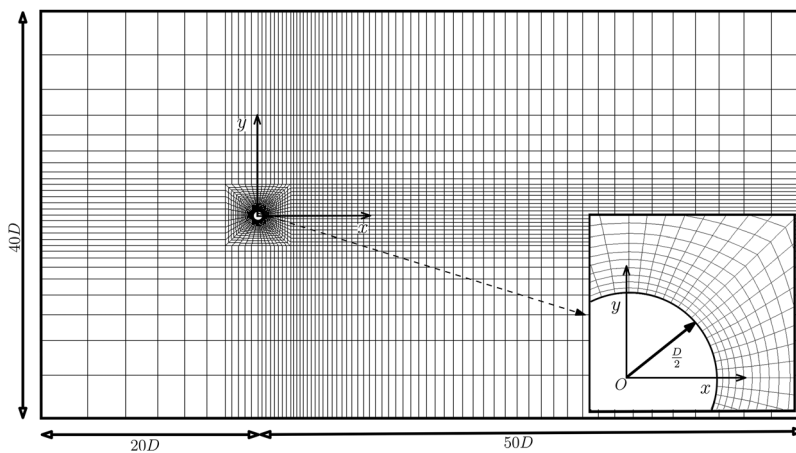


FIG. 1. Sketch of the computational domain and mesh. The streamwise-crossflow x – y plane is discretized in high-order spectral quadrilateral elements, while the spanwise direction uses a Fourier expansion. The inset shows a detail of the mesh around the cylinder and in the near wake.

tensor is defined to include fluctuations both due to von Kármán vortex shedding and the three-dimensional deviation away from it,

$$-\langle \mathbf{u}' \otimes \mathbf{u}' \rangle = - \begin{pmatrix} \langle u'u' \rangle & \langle u'v' \rangle & \langle u'w' \rangle \\ \langle v'u' \rangle & \langle v'v' \rangle & \langle v'w' \rangle \\ \langle w'u' \rangle & \langle w'v' \rangle & \langle w'w' \rangle \end{pmatrix}. \quad (4)$$

III. RESULTS

A. Global quantities

The most salient global quantities that result from our numerical simulations are listed in Table II. The statistics are deemed sufficiently converged for cases 1 through 3, while case 4 may require longer runs. Partial analysis of increasingly long time-samples shows that a bare minimum of 30–40 vortex shedding cycles are required for converged turbulent statistics. This is true of our computations at $Re = 2000$ but cannot be extrapolated to higher Reynolds numbers, which may require somewhat longer simulation times. Cases 3 and 4 have enhanced in-plane resolution with respect to 1 and 2 (5484 against 4040 seventh-order spectral elements), while spanwise resolution is highest for case 3 (~ 50 Fourier modes per spanwise unit), followed by case 1 (~ 42), case 2 (~ 32), and case 4 (~ 31). The lowest resolutions used here qualify as broadly adequate in view of the published literature, and all other parameters being kept constant, only further coarsening had an observable effect on statistics. On the other hand, increasing the spanwise size of the domain from $L_z = 1.5$ (case 1) to 2.5 (case 3) does have a noticeable impact on all global quantities, while further increase to $L_z = \pi$ has little to no effect. We will therefore focus the analysis on case 3 as it gathers the highest resolution, seemingly adequate spanwise extent, and the sufficiently long time integration that is required to produce well converged statistics.

Vortex shedding frequency $f_{vK} = 0.215$ stands in perfect agreement with experiments both at the same or nearby Reynolds number^{27,58,60} and at noticeably higher Re ,^{27,47,49,57} given that the evolution of the Strouhal number in this regime is rather flat.³¹

The mean drag coefficient has not often been reported in experiments, but our result $C_D = 0.975$ is in very close agreement with the few cases where it has.^{27,45} Consistency with numerical simulations at similar Re is also good,⁶⁴ and the somewhat higher values reported at the very common $Re = 3900$ are entirely compatible with the slightly increasing trend expected in this regime. The lift coefficient rms fluctuations $C_L' = 0.102$ fall within the range reported in the only experiments where these have been measured.⁵⁷

The distribution of the mean pressure coefficient $C_p(\theta)$ (solid line) along the cylinder wall is shown in Fig. 2(a). The stagnation point, clearly identifiable with $C_p(0) = 1$ at $\theta = 0^\circ$, is followed by a quick descent of C_p as the flow accelerates and reaches a minimum at $\theta \simeq 70.7^\circ$. Here, recompression starts and separation occurs shortly after at $\theta_{sep} = 90.0^\circ$, as indicated by the null mean friction coefficient $C_f = 2\tau_w/(\rho U_\infty)$ (dashed line; τ_w is the wall shear stress). Beyond the mean separation point, C_p keeps increasing but quickly saturates at the cylinder base value $C_{pb} = -0.80$ such that the distribution becomes flat. Meanwhile, C_f quickly recovers beyond separation except that friction acts in the upstream direction and then decreases non-monotonically down to null at the base of the cylinder. The C_p distribution compares favorably with experiments. The numerical results closely follow those of Norberg,³¹ measured

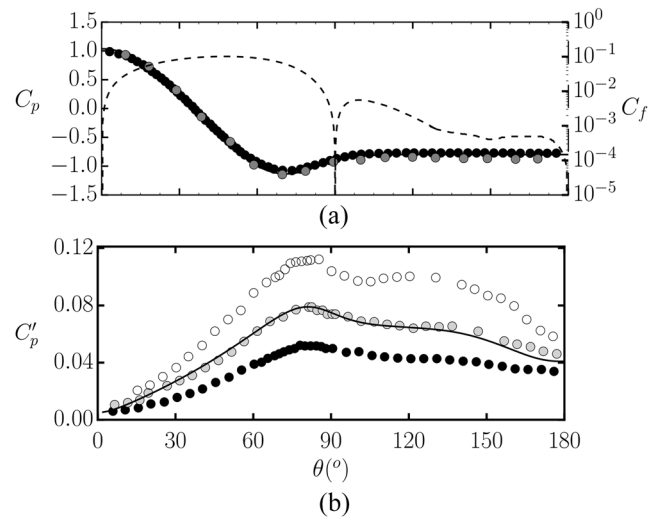


FIG. 2. (a) Mean pressure coefficient C_p (left axis, solid) and skin friction C_f (right axis, dashed) coefficient distributions on the cylinder surface. Also shown are experimental distributions of C_p by Ref. 31 (black circles: $Re = 1500$, aspect ratio 50) and Ref. 27 (dark gray circles: $Re = 3000$). (b) rms fluctuation of the pressure coefficient C_p' . Circles indicate the experimental results by Ref. 57 at $Re = 1500$ (black), 4400 (light gray), and 5000 (white).

at $Re = 1500$, while the boundary layer remains attached. The computed flat C_p distribution in the detached region falls precisely in between experiments at $Re = 1500$ ³¹ and $Re = 3000$.²⁷ The higher values reported at $Re = 3900$ obey the known increasing trend of $-C_{pb}$ beyond $Re \gtrsim 2000$.^{1,31} The rms fluctuation of the pressure coefficient C_p' is shown in Fig. 2(b). Fluctuations are almost imperceptible at the stagnation point and rise steadily along the front surface of the cylinder. They peak at $\theta \simeq 82^\circ$, just ahead of the boundary layer separation point. Beyond this point, they remain fairly high although a slight decreasing trend is observed as the cylinder base is approached. Comparison with the experiments by Norberg⁵⁷ is fair. The functional shape is closely mimicked by our numerical results, and a quantitative comparison places our $Re = 2000$ results in between the experimental results at $Re = 1500$ (black circles) and $Re = 5000$ (empty circles). Very close agreement is achieved with experiments at $Re = 4400$ (light gray circles), but whether this is a result of experimental or numerical inaccuracies or reveals actual physics consisting of a C_p' plateau in the range $Re \in [2000-4400]$ is a question that cannot be elucidated from existing data.

The separation point, at $\theta_{sep} = 90.0^\circ$, is slightly retarded with respect to numerical simulations at $Re = 3900$ reported in the literature (see Table 1). The only experimental attempt at measuring it produced a value $\theta_{sep} = 85 \pm 2$ at $Re = 3900$, while no numerical or experimental study has ever reported it for $Re = 2000$ to the authors' knowledge.

B. Near-wake topology and statistics

The near-wake mean velocity field $\bar{\mathbf{u}}(\mathbf{r}_2)$ consists in a closed recirculation bubble, as illustrated by the mean flow-field

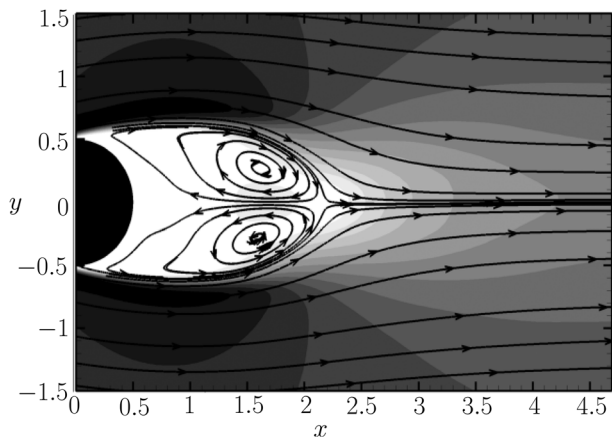


FIG. 3. Near-wake mean flow topology. Velocity magnitude contour plot, with $\|\bar{\mathbf{u}}\| \in [0.0, 1.3]$ [darker shading for higher velocity] in steps $\Delta\|\bar{\mathbf{u}}\| = 0.1$, and streamlines.

streamlines in Fig. 3. Within the enclosed recirculation bubble, delimited at the rear by a stagnation point, a symmetric vortex pair is clearly discernible. The streamline distribution compares favorably with the PIV measurements by Konstantinidis and Balabani⁶⁰ [Fig. 2(a)] for a steady cylinder at $Re = 2150$, as also do the time-averaged velocity magnitude contours. The high cross-stream gradients of the velocity magnitude along the top and bottom boundaries of the recirculation bubble indicate the presence of strong shear layers. The statistical symmetry with respect to the wake centerline is clear, which constitutes a good indicator that the data samples are sufficiently large.

Contour plots of second-order flow statistics are shown in Figs. 4(a)–4(c). The normal-streamwise [$\langle u'u' \rangle$, Fig. 4(a)] and streamwise-cross-stream Reynolds stresses [$\langle u'v' \rangle$, Fig. 4(c)] have symmetric and anti-symmetric extrema, respectively, away from the wake centerline. While $\langle u'u' \rangle_{\max}$ occurs at the rear part but still within the recirculation bubble, $\langle u'v' \rangle_{\min}$ falls right outside the bubble closure. Both Reynolds stresses peak right in the vortex formation region, and their contours extend upstream along the shear layers separated from either side of the cylinder. The maximum cross-stream normal Reynolds stress [$\langle v'v' \rangle$, Fig. 4(b)] occurs on the wake centerline just beyond the downstream boundary of the recirculation bubble. Qualitative agreement with the PIV measurements by Konstantinidis and Balabani⁶⁰ [Fig. 4(a)] is fair. The statistical symmetry of Reynolds stress distribution is also accomplished. The maximum spanwise normal Reynolds stress ($\langle w'w' \rangle$, not shown) occurs also on the wake centerline.

Table III reports extrema and streamwise location of near-wake flow-field statistics along the wake centerline, corresponding to current simulations and several experimental and numerical published results.

Cases 1 and 2, corresponding to rather short spanwise domains, feature rather small maximum velocity defect ($1 - \bar{u}_{\min}$) along the wake centerline at a location relatively close to the cylinder base, comparable to that reported in the literature at higher Reynolds numbers of $Re \approx 3900\text{--}4000$.^{48,49,54,61} Cases 3 and 4 have

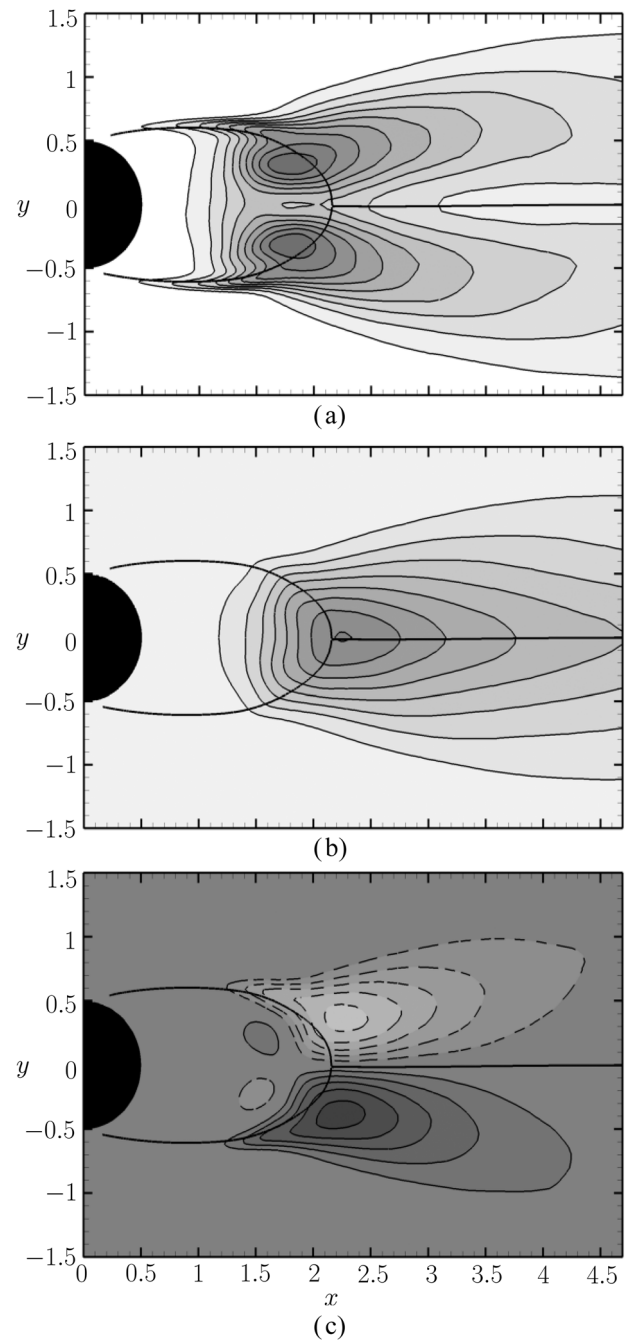


FIG. 4. Near-wake Reynolds stresses. (a) $\langle u'u' \rangle \in [0.0, 0.32]$ in steps $\Delta\langle u'u' \rangle = 0.02$, (b) $\langle v'v' \rangle \in [0.0, 0.85]$ in steps $\Delta\langle v'v' \rangle = 0.05$, and (c) $\langle u'v' \rangle \in [-0.2, 0.2]$ in steps $\Delta\langle u'v' \rangle = 0.02$. Solid (dotted) lines correspond to positive (negative) contours. The black thick line delimits the recirculation bubble.

instead $x_{\bar{u}}$ at locations perfectly compatible with experiments at nearby Reynolds numbers,⁴⁸ although $|\bar{u}_{\min}|$ seems to be a little low. Centerline streamwise normal Reynolds stresses ($\langle u'u' \rangle$) show the expected double-peak distribution, with the first peak

TABLE III. Peak values of flow field statistics along the wake centerline. Double-valued streamwise normal Reynold stress columns ($\langle u'u' \rangle_{\max}$ and $x_{\langle u'u' \rangle}$) denote double-peak or inflection plus peak distribution. Inflection points are given in parentheses.

Author (references)	Case	Re	\bar{u}_{\min}	$x_{\bar{u}}$	$\langle u'u' \rangle_{\max}$	$x_{\langle u'u' \rangle}$	$\langle v'v' \rangle_{\max}$	$x_{\langle v'v' \rangle}$	$\langle w'w' \rangle_{\max}$	$x_{\langle w'w' \rangle}$
Present results	Case 1		-0.242	1.520	(0.084)/0.108	(1.466)/2.016	0.392	2.267	0.081	1.832
	Case 2		-0.266	1.580	(0.083)/0.108	(1.466)/2.027	0.401	2.245	0.083	1.867
	Case 3		-0.318	1.672	0.082/0.082	1.523/2.027	0.409	2.187	0.085	1.764
	Case 4		-0.302	1.718	0.086/0.087	1.504/2.004	0.373	2.245	0.093	1.764
Norberg ⁴⁸		1 500	-0.4	1.75	0.09/0.1024	1.51/2.23			0.1521	1.61
		3 000	-0.44	1.65	0.1089/0.1156	1.45/2.09			0.1296	2.08
		5 000	-0.45	1.42	0.1225/0.1296	1.23/1.83			0.1521	1.86
		8 000	-0.35	1.17	(0.1369)/0.2025	(1.02)/1.62			0.1521	1.41
		10 000	-0.38	1.04	(0.1369)/0.1849	(0.96)/1.50				
Konstantinidis <i>et al.</i> ⁵⁸		1 550			0.1089	2.1	0.2809	2.1		
		2 150			0.1024	2.1	0.2916	2.1		
		2 750			0.0961	2.1	0.3136	2.1		
		7 450			0.1225	1.5	0.4761	1.5		
Parnaudeau <i>et al.</i> ⁴⁹		3 900	-0.34	1.59	0.087	1.372				
Lourenco and Shih ⁴⁵		3 900	-0.24	0.72						
Beaudan and Moin ⁵⁰		3 900	-0.33	1.00						
Kravchenko and Moin ⁵⁴	$N_z = 48^F$	3 900	-0.37	1.4–1.5						

location and height in excellent agreement with experiments.^{48,58} The location of the second peak is also within a reasonable distance of the experimental results, but the height appears slightly low. The same occurs with the single-peak location and value of crossflow ($\langle v'v' \rangle$) and spanwise ($\langle w'w' \rangle$) normal Reynolds stresses. The location is correctly predicted, but the peak height is somewhat off.

Absolute in-plane peak values for $\langle u'u' \rangle$, $\langle v'v' \rangle$, and $\langle w'w' \rangle$, reported in Table IV, are in reasonably good agreement with the experiments by Konstantinidis *et al.*^{59,60}

Figure 5(a) shows the mean streamwise velocity distribution along the wake centerline $\bar{u}(x, 0)$. Starting from rest at the cylinder base (corresponding to $x = x_b = 0.5$), \bar{u} initially decreases into

negative, reaches a minimum at about $x \sim 1.5$, and then quickly recovers in the near-wake, leaving a velocity deficit of around $1 - \bar{u}(x, 0) \sim 0.3$ that is very slowly further recovered in the mid- and far wakes. The region where $\bar{u}(x, 0) < 0$ delimits the streamwise extent of the mean recirculation bubble such that the recirculation bubble length L_r is obtained from $\bar{u}(x_b + L_r, 0) = 0$. This is not to be confused with wake formation length, defined as $L_f \equiv \text{argmax}_x[\langle u'u' \rangle(x, 0)] - x_b$. Our numerical results (case 3) follow a trend that is fully compatible with the experiments by Norberg,⁴⁸ except that their minima seem to reach fairly lower values (see Table III). The location of the minimum for our $Re = 2000$ computation occurs precisely within the range set by the experiments at $Re = 1500$ and 3000 . The experiment by Konstantinidis *et al.*⁵⁸ at

TABLE IV. Peak values of off-centerline near-wake flow field statistics.

Author (references)	Case	Re	\bar{u}_{\min}	$x_{\bar{u}}$	$\langle u'u' \rangle_{\max}$	$x_{\langle u'u' \rangle}$	$\langle v'v' \rangle_{\max}$	$x_{\langle v'v' \rangle}$	$\langle u'v' \rangle_{\max}$	$x_{\langle u'v' \rangle}$	$\langle w'w' \rangle_{\max}$	$x_{\langle w'w' \rangle}$
Present results	Case 1	2000			0.211	1.691	0.392	2.267	-0.106	2.112	0.081	1.832
	Case 2				0.206	1.751	0.401	2.245	0.108	2.146	0.083	1.867
	Case 3				0.180	1.736	0.409	2.187	0.1059	2.269	0.085	1.764
	Case 4				0.177	1.803	0.373	2.245	0.111	2.215	0.093	1.764
Konstantinidis <i>et al.</i> ⁵⁹		2160			0.15		0.32		0.09			
Konstantinidis and Balabani ⁶⁰		2150			0.16		0.33		0.09			
Parnaudeau <i>et al.</i> ⁴⁹					0.114	??						
Dong <i>et al.</i> ⁶¹	PIV	4000	-0.252	1.5	0.2025	1.55			0.11	2.05		
	DNS	3900	-0.291	1.35	0.1806	1.72			0.14	1.90		
Lehmkuhl <i>et al.</i> ⁵⁶	Mean	3900	-0.261	1.396	0.237	1.576	0.468	2.00	-0.125	1.941		
	L		-0.323	1.590	0.223	1.723	0.441	2.105	-0.126	2.107		
	H		-0.233	1.334	0.270	1.489	0.520	1.922	-0.136	1.941		

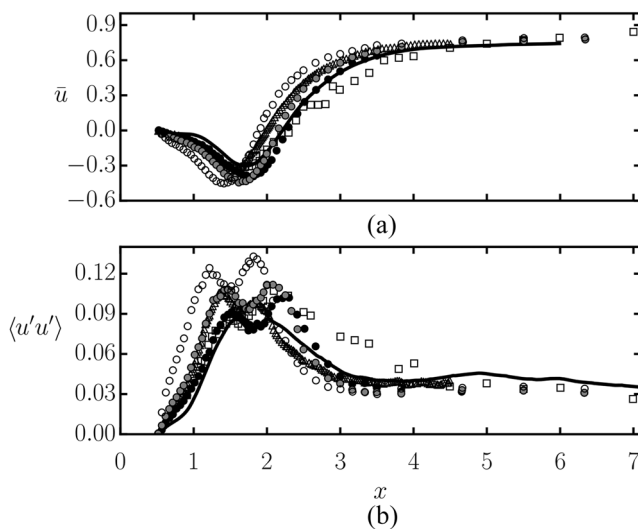


FIG. 5. Recirculating region characteristics along the wake centerline: (a) mean streamwise velocity (\bar{u}) profile and (b) Reynolds streamwise normal stress ($\langle u'u' \rangle$) profile along the wake centerline. Shown are case 3 (solid line); experiments by Norberg⁴⁸ (circles: full black: $Re = 1500$, dark gray: $Re = 3000$, empty: $Re = 5000$), Konstantinidis *et al.*⁵⁸ (squares: 2150) and Parnaudeau *et al.*⁴⁹ (triangles: $Re = 3900$).

$Re = 2150$, instead, features minima very close to our numerical results, although the data display significant scatter and the velocity defect recovery appears unusually slow. It must be borne in mind that preturbulence levels were particularly high in these experiments. The experiment by Parnaudeau *et al.*⁴⁹ at $Re = 3900$ shows also minimum $\bar{u}(x, 0)$ and a recovery rate similar to those in our numerics, while at the same time, the minimum is located halfway between the minima of Norberg⁴⁸ for $Re = 3000$ and 5000.

The comparison of the streamwise distribution of the streamwise velocity fluctuation autocorrelation [streamwise normal Reynolds stress $\langle u'u' \rangle(x, 0)$] along the wake centerline, shown in Fig. 5(b), is somewhat less straightforward. While Norberg⁴⁸ reported two-peak distributions, typical of U-type wake states, that shift to lower x and higher maxima as Re is increased, Konstantinidis *et al.*⁵⁸ presents the inflection plus peak distribution that is characteristic of V-type states. The recovery tails of the latter are also longer, possibly due to high preturbulence levels. The distal peak in the double-peak distributions of Norberg⁴⁸ is higher than the proximal peak, the dissymmetry being larger at the lowest $Re = 1500$. Parnaudeau *et al.*⁴⁹ also observed a double-peak distribution at $Re = 3900$, but the first peak rises slightly above the second in this case. The $\langle u'u' \rangle(x, 0)$ distribution in our numerical simulations on the two largest spanwise domains employed (cases 3 and 4) seems closer to that of Parnaudeau *et al.*⁴⁹ than that of Norberg⁴⁸ or Konstantinidis *et al.*,⁵⁸ even though the latter explored Reynolds numbers closer to ours. When shorter spanwise domains are used, however, the distributions tend to the inflection plus peak characteristic shape. This is in overt contradiction with prior observations that the U-type state is favored by smaller spanwise domains. The issue remains unexplained.

The agreement with experiments is fair in the mid-wake and beyond as cross-stream profiles of velocity components and Reynolds stresses at various locations $x \geq 3$ confirm (not shown). Computationally obtained profiles overlap reasonably with experimentally measured^{47,59} and numerically computed^{50,53,64,69} distributions.

The categorization of the near-wake state into U- or V-type is based on the cross-stream profile of streamwise velocity at a precise streamwise location: $\bar{u}(1, y)$. As already stated in Sec. I, every shape ranging from a clear-cut U to a sharp V has been reported in the literature. Figure 5 points at a gradual evolution of wake statistics as Re is increased but at the same time unveils high sensitivity to experimental conditions. While the size of the recirculation bubble in the near wake seems to evolve smoothly with Re for a given experimental setup, different experiments report dissimilar bubble sizes at the same exact Re such that comparing cross-stream velocity distributions at a fixed location is at the very least deceptive. The effect of experimental conditions or numerical details can, to a great extent, be accounted for with an offset in Re . Comparison at a location defined in relative terms appears thus as a much sounder approach. The results compared in this way cannot be expected to match exactly since not only the size but also the topology of the recirculation bubble evolves with Re . Accordingly, the transformation from one experiment and Reynolds number to another can only partially be explained in terms of a mere streamwise scaling or shift. We choose here to scale the x coordinate to align the location $x_{\bar{u}}$ of the minimum \bar{u}_{\min} of \bar{u} .

Figure 6 shows cross-stream velocity profiles of streamwise (\bar{u}) and cross-stream (\bar{v}) velocities at $x = 1, 1.5, 2$ for Ref. 48 and Ref. 59 and at nearby locations $x = 1.06, 1.54, 2.02$ for Ref. 49. Statistically averaged profiles are expected to be reflection-symmetric with respect to the wake centerline: $[\bar{u}, \bar{v}](x, y) = [\bar{u}, -\bar{v}](x, -y)$. Failure to preserve this symmetry would indicate lack of symmetry in the experiment (or in the measurement probe locations) or, alternatively, poorly converged statistics due to insufficient data. In this sense, the degree to which the symmetry is accomplished acts as a metric for the quality of the results. Although the degree of asymmetry in the raw simulation data was already small, we have chosen here to symmetrize numerically obtained profiles as a means of doubling the data sample size. The cross-stream profiles of streamwise velocity \bar{u} evolve from a U shape very close to the cylinder base ($x \approx 1$) toward a V shape as we move backward within the near-wake ($x \approx 2$). This alone illustrates how U- or V-shaped profiles can be obtained at will by adequately shifting the sampling location. Wakes that are topologically identical but have slightly different recirculation bubble lengths will produce very different results if the same location is chosen for comparison. As a matter of fact, our raw data feature slightly flatter profiles at $x = 1$ and $x = 1.5$ and somewhat lower velocities at $x = 2$ when compared with those of Parnaudeau *et al.*⁴⁹ When sampling locations are corrected for recirculation bubble size, the agreement is remarkable despite the significant disparity in Reynolds number ($Re = 2000$ here against $Re = 3900$ for the experimental data). Remaining discrepancies can be safely ascribed to this fact and also to mild experimental inaccuracies, as evidenced by a slight asymmetry in the profiles. Something similar occurs when analyzing cross-stream velocity profiles \bar{v} in Fig. 6(b). The significant deviations observed at $x = 1$ and 1.5, with much

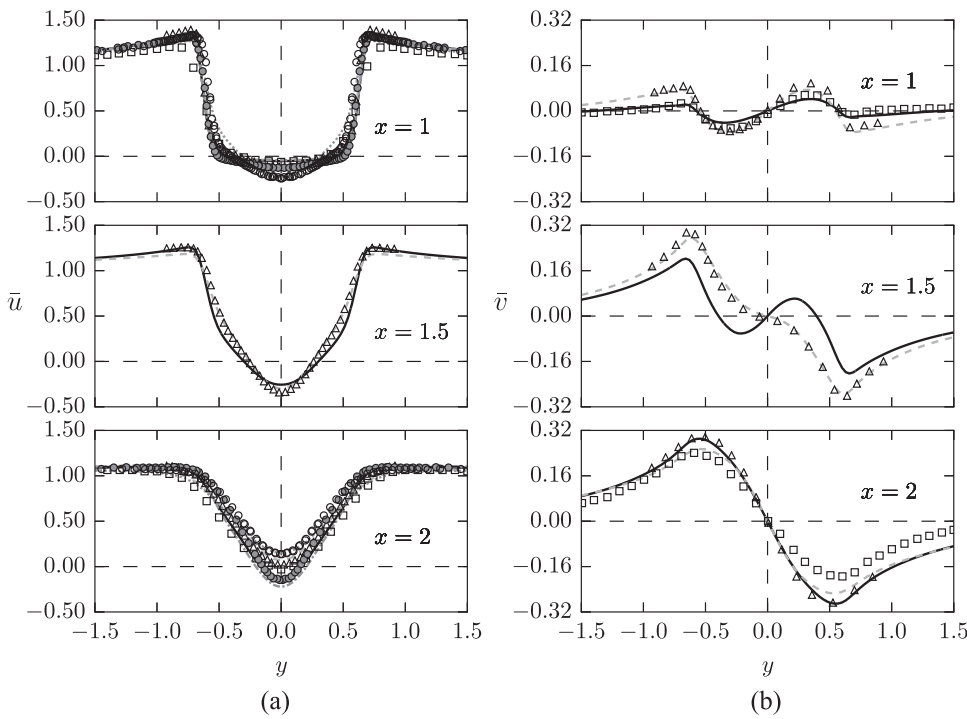


FIG. 6. Cross-stream profiles of mean (a) streamwise \bar{u} and (b) cross-stream \bar{v} velocities in the near wake. Sampling locations are $x = 1$ (top), $x = 1.5$ (middle), and $x = 2$ (bottom). Shown are case 3 (solid line); experimental results by Konstantinidis *et al.*⁵⁹ (squares, $Re = 2160$), Norberg⁴⁸ (dark gray circles: $Re = 3000, 3500$; open circles: $Re = 5000$), and Parnaudeau *et al.*⁴⁹ (triangles, $Re = 3900$, at nearby locations $x = 1.06, 1.54, \text{ and } 2.02$); numerical results corrected for Norberg⁴⁸ (gray dashed-dotted line, $Re = 3000, 3500$; gray dotted line $Re = 5000$) and for Parnaudeau *et al.*⁴⁹ (gray dashed line).

flutter profiles, are fully resolved upon correction. At $x = 2$, the agreement was already good prior to correction and scaling weakens the agreement. The different wake topologies are to be held responsible for this.

Taking Ref. 48 as a baseline for comparison, bubble length correction of simulation results yields fairly good recovery of \bar{u} profiles at both $Re = 3000$ and 5000 , while no experimental data are available for \bar{v} . Finally, the numerical bubble size is sufficiently close to

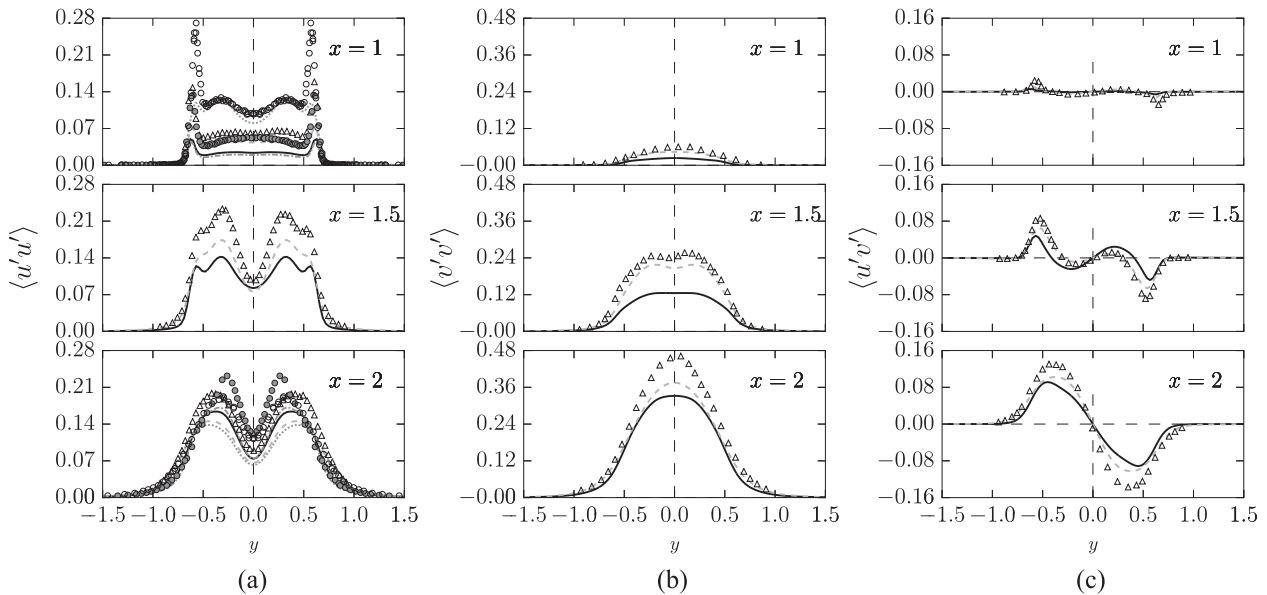


FIG. 7. Cross-stream profiles of Reynolds stresses (second-order moments) in the near wake. (a) Streamwise $\langle u'u' \rangle$ and (b) cross-stream $\langle v'v' \rangle$ velocity fluctuation self-correlations. (c) Streamwise-cross-stream velocity fluctuation cross correlations $\langle u'v' \rangle$. Styles and symbols as in Fig. 6.

that obtained at $Re = 2160$ by Konstantinidis *et al.*⁵⁹ so that the correction to be applied is almost imperceptible. The agreement is fair at all locations for \bar{u} and all but $x = 2$ for \bar{v} , where the experiments produced a slightly flatter profile than observed in the numerics.

Cross-stream profiles of second-order moments, i.e., Reynolds stresses, are shown in Fig. 7. Streamwise velocity fluctuation self-correlations $\langle u'u' \rangle$ display the double-peak shape (with nearly fluctuation-free wake core) at $x = 1$ that is characteristic of the U-type wake state. Two distinct phenomena are responsible for these peaks, which are located on the top and bottom boundaries of the recirculation bubble. On the one hand, the shear layers resulting from boundary layer detachment at either side of the cylinder flap synchronously due to the von Kármán instability and the associated shedding of alternate counter-rotating vortices. On the other hand, these same shear layers are subject to turbulent transition, with the ensuing occurrence of turbulent fluctuations. As we progress downstream within the near-wake, the amplitude increase of the shear layer flapping results in the diffusion of Reynolds stresses such that the peaks broaden and drift toward the wake centerline as fluctuations gradually penetrate the recirculation bubble core. The $\langle u'u' \rangle$ profile shape compares favorably with the experiments by Parnaudeau *et al.*,⁴⁹ but the levels are significantly lower for the numerical data, particularly so in the very near-wake. Correction for recirculation bubble size acts in the right direction by lifting the plateau around the wake centerline to comparable levels, but peak values remain low. Contrasting with the experimental data by Norberg⁴⁸ at $Re = 3000$ ($x = 1$) and $Re = 3500$ ($x = 2$), the numerics also qualitatively capture the right functional shape but quantitatively fall short of experimental values. In this case, correction does not improve the situation as the minimum of \bar{u} for numerics and experiments is already aligned and the scaling factor is very close to unity. Nonetheless, while it is not surprising that turbulent fluctuation levels are higher at the higher Re at which the experiments were done, the outline of the profiles is properly captured by the numerics. The exact same reasoning applies to cross-stream velocity self-correlations [Fig. 7(b)] and streamwise-cross-stream cross correlations [depicted in Fig. 7(c)], for which only the experimental data of Parnaudeau *et al.*⁴⁹ are available. Once again, qualitative agreement is excellent, while quantitative match is improved by correction but remains elusive. There is a reasonable explanation to the level mismatch in second-order statistics. Peak values of Reynolds stresses occur within the shear layers developing at either side of the cylinder, and turbulence levels in this region are naturally dependent on shear layer thickness, which in turn scales with the Reynolds number. Quantitative agreement is therefore not to be expected.

IV. DISCUSSION

A. Shear layer instability

Planar steady shear layers may be subject to the Kelvin–Helmholtz instability. In the case of the transitional flow past a cylinder, the shear layers resulting from boundary layer separation are neither planar nor steady. The Kármán instability induces a flapping motion of the wake, and a secondary instability of the von Kármán street introduces a spanwise modulation that propagates upstream in the wake and reaches, to some degree, the immediate

vicinity of the cylinder. Notwithstanding this, shear layer instability has been observed in the cylinder near wake. The precise critical value Re_{KH} (or Re_{SL}) for the inception of the Kelvin–Helmholtz (or shear layer) instability is largely dependent on extrinsic factors such as end boundary conditions, background disturbance intensity, and preturbulence levels.²⁸ For an experimental setup favoring parallel shedding conditions, the instability might occur as early as $Re_{KH} = 1200$, while oblique shedding pushes the shear layer instability to $Re_{KH} = 2600$. The instability, when present, emerges as a spatially developing train of small scale vortices characterized by velocity fluctuations of a frequency that is substantially higher than that of Kármán vortices. Kelvin–Helmholtz vortices are continuously being generated early on in the shear layer and grow as they are advected downstream. When they reach the Kármán vortex formation region, a number of them accumulate, coalesce, and are swallowed into the forming wake vortex. Using theoretical scaling arguments for the separating boundary layer on the cylinder walls and the ensuing shear layers to fit experimental data from several sources, Prasad and Williamson²³ suggested a power law $f_{KH}/f_{VK} = 0.0235Re^{0.67}$, relating the shear layer $f_{SL} \equiv f_{KH}$ and von Kármán f_{VK} shedding frequencies.

A velocity probe strategically located in the shear layer at $(x, y, z) = (0.8, 0.6, 1.25)$ clearly detects the flapping motion of the wake for most of the time, as shown by the low-frequency-low-amplitude oscillation of the cross-stream velocity v in the inset of Fig. 8. The signal, however, experiences occasional sudden bursts of much higher frequency and amplitude. Averaging the individual spectra of 64 velocity signals measured for a time lapse in excess of 20–25 vortex shedding cycles along a probe array at $(x, y) = (0.8, 0.6)$ results in the average spectrum shown in Fig. 8. Alongside the distinct vortex shedding fundamental frequency f_{VK} and its first harmonic, a broad-band low amplitude peak f_{KH} is discernible. This peak corresponds to the shear layer instability, and although the associated velocity fluctuations are large, its moderate amplitude results from the phenomenon occurring only occasionally. The peak is located at $f_{KH} \approx 3.902f_{VK}$, which falls right on top of the power law advanced by Prasad and Williamson.²³

In order to suppress the von Kármán-related oscillation from the probe array readings and thus isolate the shear layer oscillation, the signals have been processed with a high-pass fifth-order

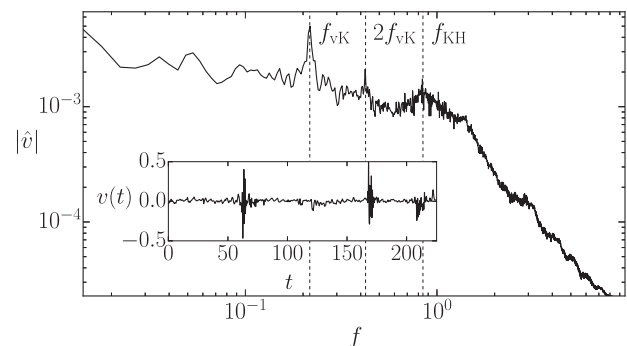


FIG. 8. Average spectrum of the crossflow velocity signals along a probe array located in the shear layer at $(x, y) = (0.8, 0.6)$. The inset shows one such signal for the probe at $(x, y, z) = (0.8, 0.6, 1.25)$.

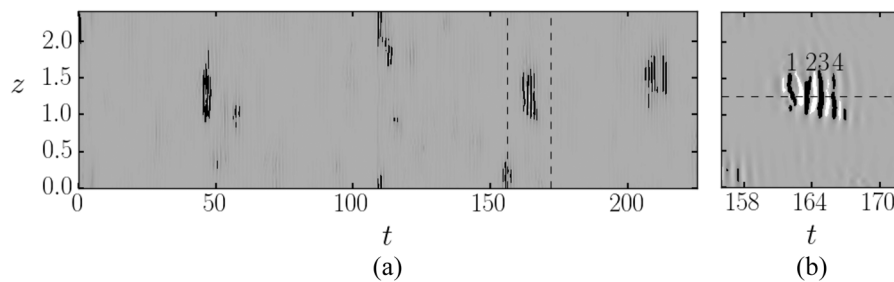


FIG. 9. Space–time diagram of filtered crossflow velocity v at $(x, y)=(0.8, 0.6)$. (a) Full time series. (b) Detail of the interval $t \in [158, 172]$ [indicated with dashed lines in panel (a)] showing the passage of Kelvin–Helmholtz vortices. The horizontal and vertical dashed lines indicate the (z, t) coordinates drawn in Fig. 10. Labels 1, 2, 3, and 4 indicate stripes that correspond to consecutive shear-layer vortices traversing the location of the probe array.

Butterworth filter with cutoff frequency $f_c = 0.7$. The filtered signals are displayed as space–time diagrams in Fig. 9. While there are no traces of the von Kármán frequency, which has been effectively filtered, occasional velocity oscillations are clearly observed as ripples that are elongated, albeit localized, in the spanwise direction. Very low amplitude ripples are perceptible here and there, but only a few grow to remarkably high amplitude. These oscillations are consistent with the passage of small spanwise vortices resulting from a Kelvin–Helmholtz instability of the shear layer, but the incipient three-dimensionality of the flapping shear layer restrains their spanwise extent, which remains always well below $1D$. This does not preclude that, at higher Reynolds, shear layer vortices become more elongated in the spanwise direction, thus preserving better two-dimensionality, as observed by Prasad and Williamson.²³ The intensification of the Kelvin–Helmholtz instability renders it perceptible further upstream on the shear layers, out of reach of the wake three-dimensionalization occurring downstream. The intermittency factor at the probe location, defined as the fraction of the time that high frequency oscillations are present, is $\gamma \approx 6$, although much longer time series would be required to obtain converged values.

Figure 10 depicts cross-sectional streamlines at $z = 1.25$ of the instantaneous velocity field at $t = 165.7$, showing four consecutive shear-layer vortices duly numbered and labeled in Fig. 9. Vortices 1, 2, and 3 have already traversed the sampling probe location (cross sign), while vortex 4 is headed toward it.

B. Secondary instability of Kármán vortices

The cylinder wake is three-dimensional from Reynolds numbers as low as $Re \lesssim 190$ ¹⁶ following well established secondary instabilities of von Kármán vortices.^{10,17} Here, we are interested in the remnants of these instabilities at a much higher Reynolds number $Re = 2000$, for which von Kármán vortices remain the dominant structure in the wake but are perturbed by spanwise modulation and superimposed spatiotemporal turbulent fluctuations.

In order to analyze the three-dimensional nature of the flow, we have followed Mansy *et al.*³³ in decomposing the flow field in a primary [two-dimensional, $\mathbf{u}_2(\mathbf{r}_2; t) = \bar{\mathbf{u}}(\mathbf{r}_2) + \mathbf{u}'_2(\mathbf{r}_2; t)$] and a secondary [three-dimensional, $\mathbf{u}_3(\mathbf{r}; t)$] component. In the restricted spanwise extent of the computational domains employed, there is no room for the development of oblique shedding or vortex

dislocation such that this decomposition does indeed properly separate all three-dimensional effects from primary vortex shedding.

Figure 11(a) shows the spacetime diagram of streamwise velocity u for a probe array located beyond the vortex formation region

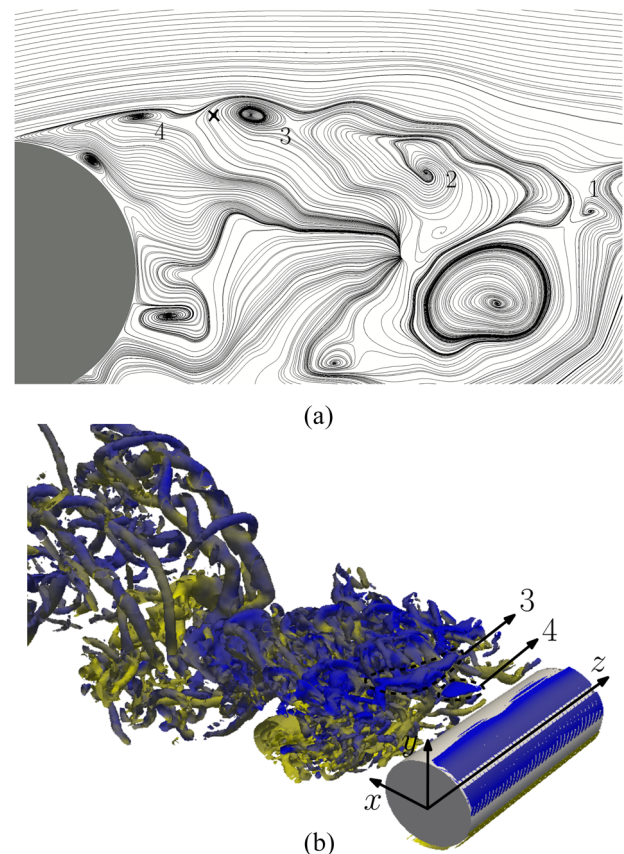


FIG. 10. Kelvin–Helmholtz instability in the shear-layer. (a) Streamlines of the instantaneous velocity field at $z = 1.25$ and $t = 165.7$, as indicated in Fig. 9. The cross indicates the location of the probe. The labels indicate consecutive shear-layer vortices. (b) Visualization of shear-layer vortices using the Q-criterion with value 5; coloring by spanwise vorticity $\omega_z \in [-10, 10]$.

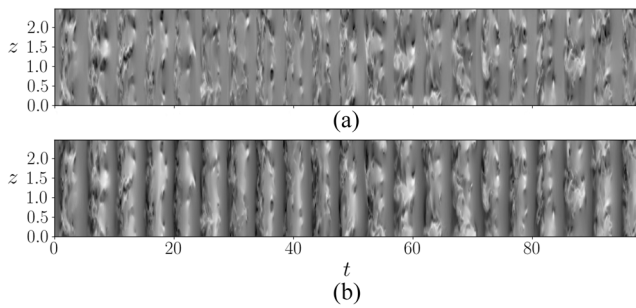


FIG. 11. Spacetime diagrams of streamwise velocity at $(x, y) = (3, 0.5)$ for (a) the total (primary and secondary combined) $u = u_2 + u_3$ and (b) the secondary flow u_3 .

at $(x, y) = (3, 0.5)$. A vertical-banded pattern, associated with vortex shedding, is clearly distinguishable. The effect of subtracting the primary flow from the total flow, yielding the secondary flow in isolation, is shown in Fig. 11(b). It is clear from the alternate homogeneous and inhomogeneous stripes that three-dimensionality is concentrated at certain phases along the vortex shedding cycle.

The spectra of the primary u_2 , and rms secondary $u_3^{\text{rms}} \equiv \sqrt{\langle u_3^2 \rangle_z}$ streamwise velocity signals are shown in Fig. 12(a). As expected, the primary signal has a clear peak at the Strouhal frequency, and two higher harmonics are also discernible. The secondary signal is somewhat flatter, but protrusions at the Strouhal frequency and a couple of harmonics are still visible, which indicates that the signals are coupled. The cross-spectral-density S_{23} of the primary and secondary signals is shown in Figs. 12(b) top and bottom to analyze the cross correlation or coherence between the signals. There is a clear peak of the cross-spectral-density modulus ($A_{23} \equiv |S_{23}|$, top panel) at precisely the Kármán frequency, indicating that the energy contents at this frequency of both signals are correlated. The cross-spectral-density phase [$\varphi_{23} \equiv \arg(S_{23})$] reveals an associated phase lag $\varphi_{23}(f_{\text{vK}}) \approx 225^\circ$. Since the primary signal peaks upon the crossing of the Kármán vortex through the sampling location, the detected phase lag implies that three-dimensionality is maximum in the trailing portion of the braid region that connects counter-rotating consecutive vortices.

Figure 13 illustrates the location of maximum three-dimensionality with two snapshots of the spanwise vorticity field that are apart by exactly $\varphi_{23}(f_{\text{vK}})$ along one vortex shedding cycle. The first one corresponds to a maximum of the primary signal as recorded at the sampling location (cross), which is being traversed by a Kármán vortex. The second one, taken $\varphi_{23}(f_{\text{vK}})$ later, shows that the sampling location is right at the braid region in between consecutive vortices. This is consistent with the short-wavelength mode B observed in the cylinder wake at much lower Reynolds numbers, as the instability leading to it is known to nucleate at the braid shear layers,^{10,75} while Mode A results from the instability of the vortex core regions. Strong counter-rotating streamwise vortex pairs can be detected in the braid regions every now and then, but the spanwise periodic pattern of mode B has long been disrupted such that vortices appear in isolation or with irregular spacing at best. The streamwise coherence of mode B streamwise vortices at onset, which

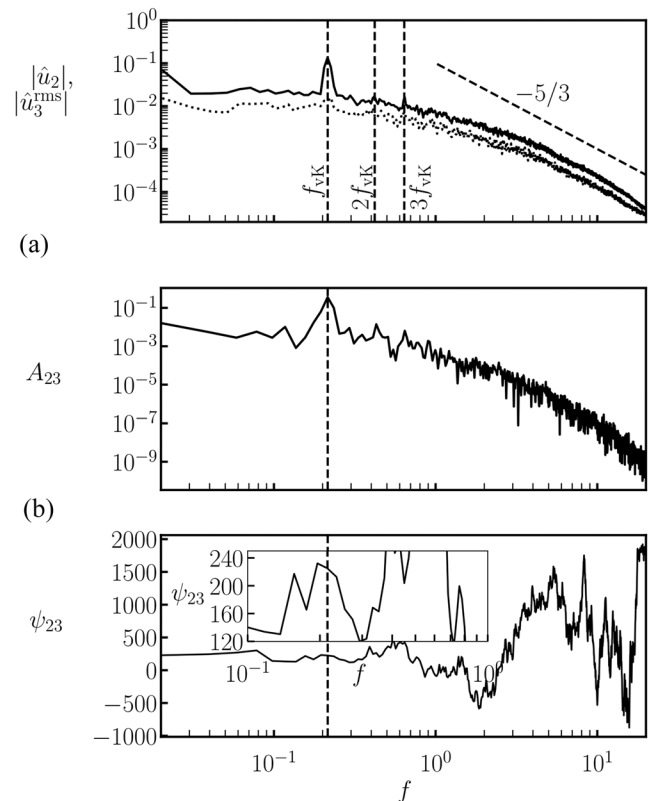


FIG. 12. (a) Spectra of the primary (u_2 , continuous line), and rms secondary (u_3^{rms} , dotted line) flow components of the streamwise velocity signal at $(x, y) = (3, 0.5)$. (b) Cross-spectral-density S_{23} of the primary u_2 and secondary u_3^{rms} signal pair [top: cross-modulus $A_{23} \equiv |S_{23}|$, bottom: cross-phase $\varphi_{23} = \arg(S_{23})$].

accounted for a characteristic symmetry from one braid to the next of opposite sign, is lost once turbulence sets in. Two-dimensional (time and z -coordinate) cross correlation of u_3 signals taken along probe arrays at $(x, y) = (3, 0.5)$ and $(x, y) = (3, -0.5)$ fail to produce the clear peak one would expect for space-time drifts $(\zeta, \tau) = (0, \pi/f_{\text{vK}})$ if mode B symmetry was preserved. The effect of turbulent transition is that of decorrelating any two signals separated by relatively short time or streamwise distance.

C. Spanwise length scale of large coherent three-dimensional structures

Quantification of the spanwise length scale of the large coherent three-dimensional structures that are present in the wake requires monitorization of some quantity along spanwise lines. Particularly useful are signals that cancel out exactly for two-dimensional vortex-shedding as their mere deviation from zero is a sign of three-dimensionality. Fourier spectral differentiation has been employed along spanwise probe arrays to compute $\tilde{\omega}_y = \frac{\partial u}{\partial z}$, as an indicator of cross-stream vorticity. The usual approach of computing spanwise self-correlation or performing Fourier analysis works fine for spanwise(-pseudo)-periodic flow structures but fails whenever the

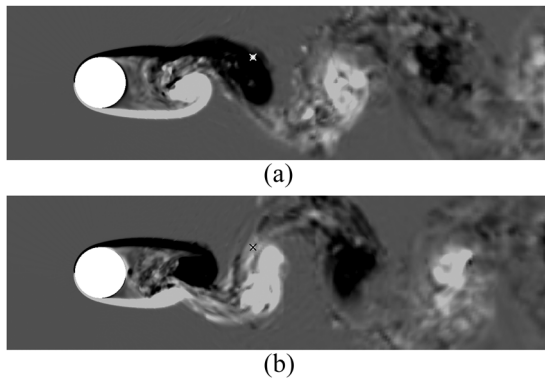


FIG. 13. Instantaneous spanwise vorticity ω_z field snapshots at (a) a maximum of the primary signal u_2 as measured by the sampling probe at $(x, y) = (3, 0.5)$ and (b) a phase $\varphi_{23}(f_{vK}) = 225^\circ$ later corresponding to a maximum of the secondary signal u_3^{rms} .

structures appear in isolation or show some localization features. The reason is that self-correlation and Fourier transforms act globally on the signal and provide global information such that structure spacing rather than size can be detected. A powerful tool for analyzing the local spectral features of a signal is the Hilbert transform. Spectrograms, wavelet transforms, and the Hilbert–Huang transform are alternative means, but the simplicity and versatility of the Hilbert transform make it more suitable for the analysis of spanwise length scales in the cylinder wake.³⁸ The Hilbert transform of a real-valued function $f(z)$ is defined by its convolution with $1/(\pi z)$ as

$$\mathcal{H}[f(z)] = \frac{1}{\pi} \int_{-\infty}^{\infty} \frac{f(\zeta)}{z - \zeta} d\zeta,$$

where the improper integral must be understood in the Cauchy principal value sense. The complex-valued function $f_a(z) = f(z) + i\mathcal{H}[f(z)]$ is the analytic representation of $f(z)$, and its modulus and argument, advisedly named local (instantaneous if the independent variable is time) amplitude and phase, respectively, provide insight into the local (instantaneous) properties of the original signal.

Thus, the analytic signal $\tilde{\omega}_y^a(z, t)$ is obtained from $\tilde{\omega}_y(z, t)$ and $\mathcal{H}_{\tilde{\omega}_y}(z, t)$ as the complex function,

$$\omega(z, t) \equiv \tilde{\omega}_y^a(z, t) = \tilde{\omega}_y(z, t) + i\mathcal{H}_{\tilde{\omega}_y}(z, t) = A_\omega(z, t)e^{i\varphi_\omega(z, t)}.$$

Its modulus $A_\omega \equiv |\omega|$ and argument $\varphi_\omega \equiv \arg(\omega)$ contain information on the local amplitude (envelope) and phase, respectively, of $\tilde{\omega}_y$. The instantaneous local spanwise wavelength of the signal is then recovered from

$$\frac{2\pi}{\lambda_z(z, t)} = \frac{d\varphi_\omega}{dz}.$$

The probability density function (PDF) of λ_z has been computed via Normal/Gaussian kernel density estimation with a bandwidth $\Delta z = 0.04$ and scaled by the mean instantaneous envelope $\langle A_\omega \rangle_z(t)$ so as to account for the energy level contained in the most predominant three-dimensional structures.

Figure 14 presents the time evolution of the $\langle A_\omega \rangle_z$ -scaled λ_z -PDF instantaneous distributions as processed from the readings obtained using the probe array located at $(x, y) = (3, 0.5)$. The shading denotes the instantaneous probability distribution of λ_z , with darker regions corresponding to the most recurrent length scales of energetic spanwise structures. Long wavelength structures are rare, as evidenced by the predominance of white for large λ_z . Meanwhile, shaded regions appear for relatively low λ_z in the form of time-localized spots with a certain (pseudo-)periodicity. Energetic spanwise structures occur intermittently, with characteristic frequency (that of vortex shedding) and spanwise size distribution. The C_L signal has been superimposed to the colormap to illustrate the existing correlation between the occurrence of spanwise flow structures and the vortex shedding process. As already anticipated by the secondary flow spacetime diagram of Fig. 11, three-dimensionality occurs predominantly at certain phases of the vortex-shedding cycle, which translates into precise streamwise locations along the vortex street, namely, the braid regions in between opposite sign vortices.

The C_L signal has been used to uniquely define a phase along the vortex-shedding cycle. The Hilbert transform has been used again, this time to turn C_L into an analytical time signal $C_L^a(t) = C_L(t) + i\mathcal{H}_{C_L}(t)$ such that the phase can be obtained as $\theta(t) \equiv \arg(C_L^a(t))$. The right panel of Fig. 14 zooms into a full vortex-shedding cycle and indicates eight equispaced phases $\theta_i = 2\pi i/8$ ($i \in [0, 7]$) along it. Four distinct stages can be clearly

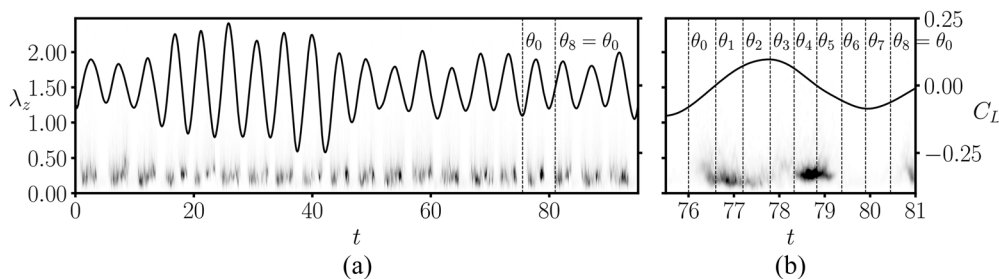


FIG. 14. Time evolution of the lift coefficient C_L (right axis) and PDF of the instantaneous spanwise wavelength λ_z distribution at $(x, y) = (3, 0.5)$, scaled by the mean instantaneous envelope $\langle A_\omega \rangle_z$ (left axis). (a) Full time-series. (b) Detail of $t \in [75, 82]$. The vertical dashed lines indicate the time instants for eight equispaced C_L signal phases $\theta_i = 2\pi i/8$ ($i \in [0, 7]$).

identified during the cycle. For around one quarter of the cycle, represented by phases θ_6 through $\theta_8 = \theta_0$, the wake has no perceptible three-dimensionality at the sampling location. Later on, three-dimensional spanwise structures of very small size start being observed at the probe array with increasing probability that peaks between phases θ_1 and θ_2 . Beyond this first probability peak, the recurrence of the structures declines to some extent, reaching a local minimum in between phases θ_3 and θ_4 . Past this stage, spanwise structures regain presence and their probability of occurrence reaches a second peak at phase θ_5 . The spanwise extent of the three-dimensional structures progressively grows as their recurrence declines from the first probability peak and bounces back toward the second peak. The most probable structures are therefore slightly larger, although still rather small, for the second peak than for the first. Beyond the second peak, three-dimensionality quickly vanishes before the cycle starts anew.

In order to substantiate the cyclic nature of the spanwise flow structures measured at a fixed (x, y) -location in the wake, phase averaging of the flow field has been undertaken. The data comprised in the interval $\theta \in [\theta_i - \pi/8, \theta_i + \pi/8]$ ($i \in [0, 7]$) of all available vortex-shedding cycles have gone into averaged phase $\bar{\theta}_i$. The resulting phase-averaged $\langle A_w \rangle_z$ -scaled PDF distributions at the off-centerline sampling location $(x, y) = (3, 0.5)$ are shown in Fig. 15. Direct time-averaging of the $\langle A_w \rangle_z$ -scaled PDF distributions (black solid line) already detects the presence, at the sampling location, of three-dimensional structures of size distributed around $\lambda_z = 0.234$. Furthermore, the evolution of the phase-averaged spanwise size distributions corroborates the observations made for the particular vortex-shedding cycle of Fig. 14. Three-dimensionality is scarce at phase θ_0 , but spanwise structures start appearing with quickly growing probability that peaks at $\bar{\theta}_2$ with prevailing spanwise size $\lambda_z \approx 0.204$. Structures become less abundant and/or less energetic for phases $\bar{\theta}_3 \sim \bar{\theta}_4$ as they grow in typical size to $\lambda_z \approx 0.219$. As the cycle progresses, spanwise structures are fast re-energized and become

more recurrent until reaching a new probability peak at phase $\bar{\theta}_5$ with spanwise size distributed around $\lambda_z \approx 0.280$. Beyond this point, ubiquity of three-dimensional structures sharply drops until becoming almost imperceptible at phase $\bar{\theta}_6$. Three-dimensionality remains insignificant for the rest of the cycle.

Spanwise-averaged flow vorticity snapshots taken at phases θ_0, θ_2 , and θ_5 are shown in Fig. 16 to identify the location along the wake where three-dimensional structures occur. Phase-averaged snapshots [Fig. 16(b)] are shown alongside instantaneous snapshots [Fig. 16(a), for the particular vortex-shedding cycle depicted in Fig. 14(b)] to convey the general recurrence of three-dimensionality at the same locations in the wake. The leading front of the Kármán vortex and the nearly quiescent flow field immediately downstream (top panel, which corresponds to phase θ_0) preserve a markedly two-dimensional character. In the downstream portion of the braid region, immediately at the vortex trailing front (middle panels, θ_2), is where the smallest highly energetic three-dimensional structures are to be identified. At the upstream part of the braid region, where it connects with the next Kármán vortex of opposite sign (bottom panels, θ_5), high energy spanwise structures of a slightly larger spanwise extent thrive. In between, in the mid-section of the braid region, three-dimensionality appears to be somewhat weaker. As a matter of fact, this is the result of the curved nature of the braid region such that its core sheet crosses the sampling location, at a fixed cross-stream coordinate, twice. It is natural to assume that the three-dimensional structures extend in fact along the braid region pretty much unaltered, just with a mild propensity to grow from the leading to trailing region. The apparent weakening would therefore be a result of the curvature of three-dimensional structures along the braids. This scrutiny of spanwise flow structures confirms the notion, already anticipated by the analysis of the primary and secondary flows, that three-dimensionality is suppressed by the strong spanwise vorticity of Kármán vortices but thrives in the trailing braid regions at a phase of 225° later, the precise phase lag that separates the most energetic spanwise structures (θ_5) from the weakest (θ_0). The inquiry into the spanwise length scale of three-dimensionality further reveals that the structures are of rather small spanwise extent and that their size experiences a periodic evolution along the vortex street.

Figure 17 shows instantaneous streamwise cross sections of cross-stream vorticity $\omega_y(3, y, z)$, containing the probe array (dashed line), at the very same times as in Fig. 16(a). The probe clearly registers quasi-two-dimensional flow at θ_0 (left panel), although three-dimensional structures are clearly visible at the symmetric y -location as a lower braid traverses the cross section at the time. At θ_2 (center panel), the upper braid downstream region traverses the cross section. In this case, a couple of vortex pairs are spotted at precisely the probe-array location. Note that a Fourier transform or signal autocorrelation along the probe would have provided the spacing between the vortex pairs rather than the local size of each one of them. The Hilbert transform works locally and will in fact produce the characteristic size of every strong vortex traversing the probe array. It must be realized that the sizes given by the Hilbert transform will correspond to that of a compact vortex pair. If, for whatever reason, the vortex pair splits into two counter-rotating vortices that drift apart, the Hilbert transform will measure the size of the original vortex pair as though the vortices had remained packed together. We thus measure double the size of individual vortices, regardless of

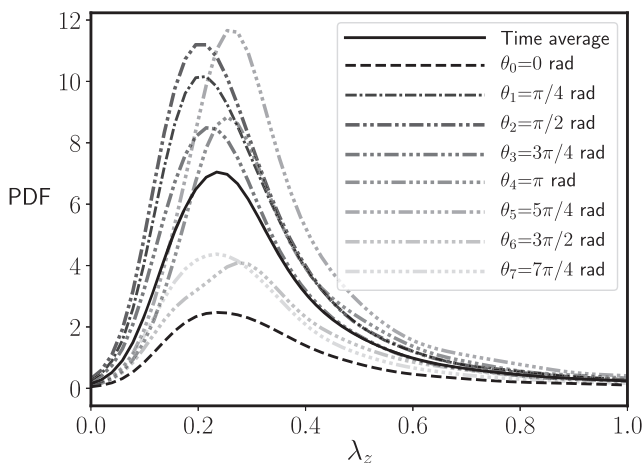


FIG. 15. Time-averaged (solid line) and phase-averaged (dashed lines, coloring as indicated in the legend) $\langle A_w \rangle_z$ -scaled PDF distributions at phases $\theta_i = 2\pi i/8$. Normal/Gaussian kernel density estimation with a bandwidth $\Delta z = 0.04$ has been employed.

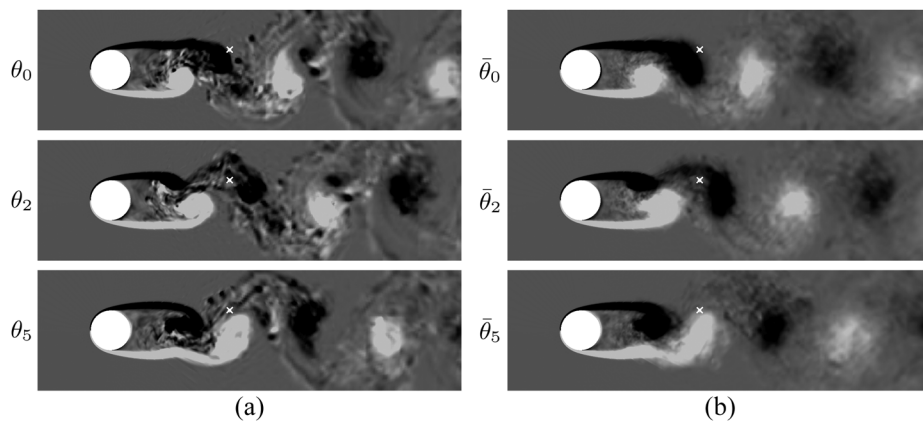


FIG. 16. Spanwise-averaged vorticity fields at phases θ_0 (top), θ_2 (middle), and θ_5 (bottom) along the vortex-shedding cycle. Vorticity is in the range $\omega_z \in [-2, 2]$, clear for positive and dark for negative. The cross indicates the sampling location of the signals in Fig. 14. (a) Instantaneous snapshots corresponding to the vortex-shedding cycle of Fig. 14(b). (b) Phase-averaged snapshots.

whether they appear in pairs or in isolation. At θ_5 (right panel), it is the upstream region of the braid that traverses the cross section. Once more, both vortex pairs and isolated vortices can indistinctly be detected at the probe array height.

At the same height but below the wake center plane (i.e., the mirror image of the probe location), three-dimensionality is weaker and less structured than in the braid core, where the strongest vortical structures of clear-cut characteristic size happen to be. We surmise that it is these latter vortices that extract energy from the main shear and constitute the primal instability that then breaks down into the featureless lower-intensity turbulence that dominates the trailing region left behind by the braids in their downstream advection. The low-intensity turbulent region in the bottom half of the θ_2 and θ_5 panels would therefore correspond to the region just cleared by a lower braid and waiting to be reached by the leading front of an oncoming Kármán vortex. A couple of final considerations regarding structure size measurement need to be mentioned at this point. First, if we consider vortex pairs as embedded inside an envelope, the instantaneous horizontal size of this envelope as measured at the

probe array will oscillate as the vortex, which has a certain streamwise tilt due to the braid slope and curvature, traverses it. From the probe, the vortex pair will be seen as either rising or descending and the correct size will only be measured when the vortex cores are at exactly the probe height. This introduces a bias in size measurement toward somewhat smaller-than-actual structures. A spanwise tilt of a vortex pair will entail a similar effect. We have employed $\bar{\omega}_y$ instead of the real vorticity ω_y for computing structure size. There is no guarantee that the sizes measured will remain the same if different signals are used. Trading some vorticity component for another or for any velocity component might produce different results. Deviations should not be enormous, but the definition of structure size is somewhat loose and can of course depend on the field used for its measurement.

In order to characterize the typical spanwise size of three-dimensional flow structures, the mode (peak) of the time-averaged $\langle A_\omega \rangle_z$ -scaled λ_z -PDF distribution, rather than the mean, has been taken as the most probable wavelength $\bar{\lambda}_z$. Due to the skewed shape of the size distributions, the mean is not a particular good

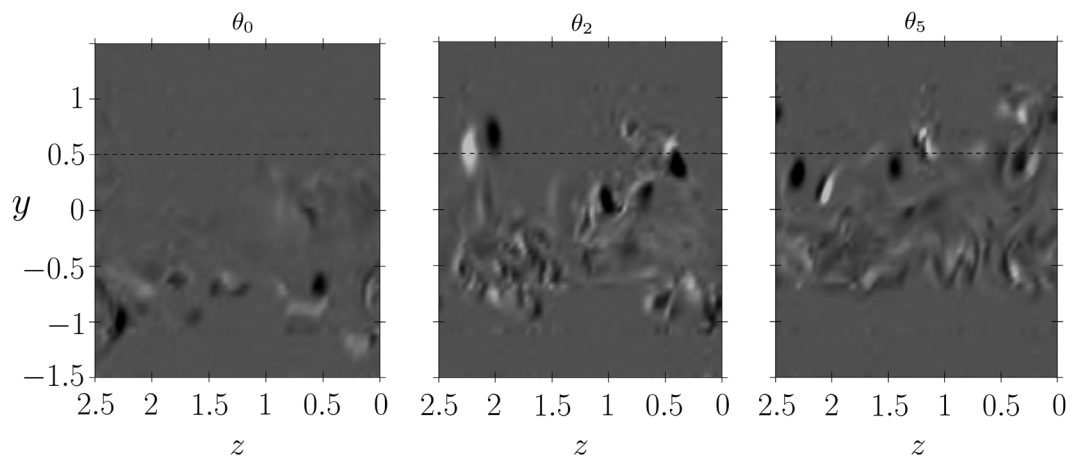


FIG. 17. Colormaps on a streamwise cross section, containing the probe array, of instantaneous cross-stream vorticity $\omega_y(3, y, z)$ at phases θ_0 , θ_2 , and θ_5 . The probe array is indicated with a dashed line.

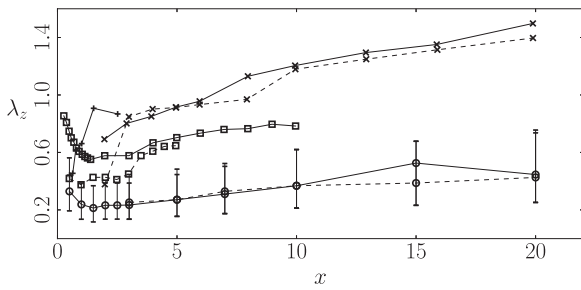


FIG. 18. Typical spanwise size λ_z of three-dimensional structures along the wake measured off-centerline at cross-stream locations $y = 0.5$ (solid lines) and $y = 1$ (dashed lines). Shown are our numerical results (circles) along with the numerical results by Gsell *et al.*³⁶ at $Re = 3900$ (squares) and experimental results by Mansy *et al.*³³ at $Re = 600$ (crosses) and Chyu and Rockwell³⁷ at $Re = 10\,000$ (plus signs). The error bars denote the range for which the probability remains above half the peak probability.

indicator of the most probable spanwise sizes. To provide a measure of distribution spread or variability, a range $[\lambda_z^{\min}, \lambda_z^{\max}]$ has been defined by picking the interval where the PDF remains above 50 of its maximum. Thus, typical positive and negative deviations have been defined as $\delta_{\lambda_z}^+ = \lambda_z^{\max} - \bar{\lambda}_z$ and $\delta_{\lambda_z}^- = \bar{\lambda}_z - \lambda_z^{\min}$, respectively.

Figure 18 shows the evolution of the typical spanwise size of three-dimensional structures along the wake. The measurements have been taken off-centerline at $y = 0.5$ and $y = 1$. The trends for $y = 0.5$ observed by Gsell *et al.*³⁸ at $Re = 3900$ using a similar analysis are recovered in the present results at $Re = 2000$, although the typical sizes were notably larger in the former study. In our case, the spanwise size of structures decreases from $\bar{\lambda}_z \approx 0.35$ in the immediate vicinity of the cylinder along the shear layers until reaching a minimum $\bar{\lambda}_z \approx 0.25$ at about $x \approx 2-3$ in the vortex formation region. The size gradually recovers afterward, asymptotically tending to $\bar{\lambda}_z \approx 0.4$ by $x = 20$. In Ref. 38, the sizes are off by over 0.4. At $y = 1$, we observe the same trends as for $y = 0.5$ and very close values from $x \gtrsim 2.5$ on. In contrast with the observations by Gsell *et al.*³⁸ at the larger $Re = 3900$, the sizes of the structures in the very near wake at this cross-stream location are meaningless as three-dimensionality is barely noticeable. This can be ascribed to the lower Re employed in our simulations. Three-dimensionality (and turbulence, for that

matter) seems to have a hard time diffusing upstream and cross-stream at $Re = 2000$ but not so much at $Re = 3900$. Comparison with the experimental results by Mansy *et al.*³³ at $Re = 600$ and Chyu and Rockwell³⁷ at $Re = 10\,000$ is hindered by the exceedingly different flow regimes considered and by the methodology employed, which we assess adequate for estimating spanwise structure spacing but not size. To any rate, Mansy *et al.*³³ reported a spanwise size $\bar{\lambda}_z \approx 0.45$ at $(x, y) = (3, 0.5)$, which is larger but not overly far from our values at the same location.

D. Spanwise spacing of streamwise vortices in the near-wake

If the three-dimensional structures were to appear in a (pseudo-)periodic spanwise pattern, one would expect to observe $N_{vp} \approx L_z/\lambda_z$ equispaced vortex pairs filling the entire spanwise extent of the domain. As we have seen, this is not the case and vortex pairs appear entirely decorrelated from one another and vortices in isolation are oftentimes observed. Figure 19(a) shows the instantaneous count of vortex pairs N_{vp} as a function of time. Vortices are counted whenever cross-stream pseudo-vorticity exceeds a certain threshold $|\bar{\omega}_y| \geq 8$ at the designated location, here $(x, y) = (3, 0.5)$. In some periods, corresponding to the traversal of Kármán vortices, no streamwise vortices are observed at all. Along the braids, isolated streamwise vortices and vortex pairs are regularly detected instead. Up to 4–4.5 simultaneous vortex pairs have been detected occasionally such that the average spanwise spacing between side-by-side pairs is $L_z/N_{vp} = 0.56-0.63$. This minimum average spacing is well above the typical vortex-pair spanwise size λ_z^{\max} reported above such that not even in these rare occasions do the three-dimensional structures appear in anything remotely resembling a periodic pattern like that observed for the A and B modes at much lower Reynolds numbers. Figure 19(b) presents in a histogram, the fraction of time $X_{N_{vp}}$ that the probe array at $(x, y) = (3, 0.5)$ detects so many (N_{vp}) simultaneous vortex pairs. Note that the unit is the vortex pair such that a vortex in isolation is counted as 1/2 and N_{vp} must necessarily take values that are a natural multiple of 0.5. Isolated vortices ($N_{vp} = 0.5$) cross the probe array just over 15 of the time and close to another 15 of the time a vortex pair (or two isolated vortices, $N_{vp} = 1$) is being detected. Larger amounts of simultaneous vortices are detected with decreasing probability. We are interested here in the continuous probability distribution of vortex spanwise spacing l_z in the case of the infinitely long cylinder, which is related to

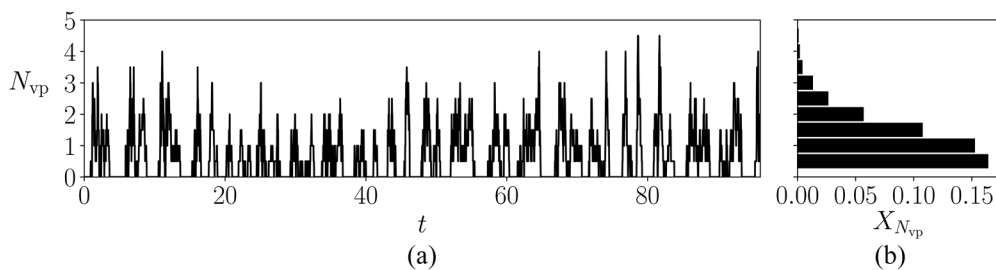


FIG. 19. Count of vortex pairs traversing the probe array at $(3, 0.5)$. (a) Time evolution of the vortex pair count. The threshold for counting the occurrence of a vortex is $|\bar{\omega}_y| \geq 8$. (b) Histogram of time fraction $X_{N_{vp}} \equiv t_{N_{vp}}/T$ of observation of N_{vp} vortex pairs. Half values result from the detection of isolated vortices.

the number of vortices in a sufficiently extended cylinder of spanwise size L_z by $l_z \equiv L_z/(2N_{vp})$. While the maximum of the PDF for l_z (l_z^{\max}) is expected to be independent of L_z for sufficiently long cylinders, the maximum of the N_{vp} -PDF (N_{vp}^{\max}) is instead foreseen as inversely proportional to the domain size. To properly reproduce the continuous distribution of l_z with a finite-span domain, one would naturally require that L_z is large enough so that the discrete distribution of N_{vp} contains the maximum N_{vp}^{\max} and the probability tails drop sufficiently at either side. The maximum can be interpreted as the preferred spanwise spacing of three-dimensional structures in the cylinder wake and, as such, acts as a threshold to how many streamwise vortices can *comfortably* be packed together per unit span. Below this spacing, streamwise vortices tend to *repel* each other by whatever mechanism, possibly unaccounted for large-scale motions. In this sense, a strict minimum L_z should at the very least fit $l_z^{\max} = L_z/(2N_{vp}^{\max})$. In our domain $L_z = 2.5$, the probability of observation of simultaneous vortices is a strictly decreasing function of the number considered, with $N_{vp}^{\max} = 0.5$ corresponding to maximum probability. This would in principle point at an insufficient domain size, but, as it happens, $L_z = 2.5$ seems to be about the minimum that captures the probability distribution correctly up to the maximum, as the saturating value of $X_{N_{vp}}$ for $N_{vp}^{\max} = 0.5$ seems to indicate. Larger domains would therefore properly capture the probability maximum and part of the decreasing trend toward lower N_{vp} , while smaller domains would be forcing the maximum to be at lower spacing values than the cylinder wake would naturally select. We believe that this may be among the reasons why insufficient spanwise domain sizes produce wrong turbulent statistics, here and in published literature results. The spanwise spacing of vortical streamwise structures, rather than their size, would therefore dictate the minimum computational domain extent. The spacing being a function of Reynolds number, no definite trend can be extracted from our computations, all of which correspond to the same unique $Re = 2000$.

E. Fastest growing three-dimensional structures

The Floquet stability analysis of the time-periodic two-dimensional flow around the cylinder has been successfully employed in the past to pinpoint the Re -regime at which three-dimensionality kicks in Refs. 17 and 36. The leading eigenmodes found are consistent with mode A observed in experiments, and the hysteresis can be ascribed to the subcritical character of the bifurcation. Meanwhile, the existence of mode B has been tracked down via Floquet analysis to a secondary bifurcation of the already unstable two-dimensional periodic vortex-shedding regime.¹⁰ These bifurcations introducing three-dimensionality to the flow occur in the range $Re \in [188.5, 260]$. If forced computationally to preserve two-dimensionality, vortex-shedding remains time-periodic for still some range of Re . At $Re = 2000$, however, periodicity has long been disrupted and two-dimensional vortex-shedding has become chaotic. It is highly debatable whether the Floquet analysis of the Kármán periodic solution at this regime can capture any of the features of the three-dimensional structures observed in experiments and in fully three-dimensional numerical simulations. Nonetheless, we have chosen here to undertake what we call pseudo-Floquet stability analysis of the underlying two-dimensional solution, which happens to be a pseudo-periodic chaotic state, to compare the fastest

growing modes with the structures that arise in direct numerical simulation. Long two-dimensional time integration has been performed to characterize the chaotic state, with velocity and pressure fields $[\mathbf{u}_2^{2D}, p_2^{2D}](\mathbf{r}_2, t)$. Random three-dimensional perturbations $\tilde{\mathbf{u}}$ of wavenumber $\beta_z = 2\pi/\lambda_z$ (λ_z is the fundamental wavelength), scaled to very low amplitude by a factor $\epsilon \sim 10^{-12}$, have been added to \mathbf{u}_2^{2D} at several randomly picked time-instants and evolved in time using a single spanwise Fourier mode in order to avoid spanwise mode interaction and, thus, allow straightforward analysis, through direct time evolution, of the modal growth/decay in the linear regime. Given that $[\mathbf{u}_2^{2D}, p_2^{2D}]$ exactly satisfy the Navier-Stokes equations, introducing the perturbation field

$$[\mathbf{u}, p](\mathbf{r}; t) = [\mathbf{u}_2^{2D}, p_2^{2D}](\mathbf{r}_2; t) + \epsilon[\tilde{\mathbf{u}}, \tilde{p}](\mathbf{r}; t)$$

results, after canceling out all terms associated with the two-dimensional solution, in

$$\frac{\partial \tilde{\mathbf{u}}}{\partial t} + (\mathbf{u}_2^{2D} \cdot \nabla) \tilde{\mathbf{u}} + (\tilde{\mathbf{u}} \cdot \nabla) \mathbf{u}_2^{2D} = -\nabla \tilde{p} + \frac{1}{Re} \nabla^2 \tilde{\mathbf{u}},$$

$$\nabla \cdot \tilde{\mathbf{u}} = 0,$$

where the nonlinear term $(\tilde{\mathbf{u}} \cdot \nabla) \tilde{\mathbf{u}}$ has been dropped as negligible from its appearing scaled by ϵ^2 .

If $[\mathbf{u}_2^{2D}, p_2^{2D}]$ were exactly periodic, Floquet theory's modal ansatz would establish that, after some initial transients t_0 , the perturbation field should evolve as

$$[\tilde{\mathbf{u}}, \tilde{p}](\mathbf{r}; t_0 + kT) = [\tilde{\mathbf{u}}_0, \tilde{p}_0](\mathbf{r}) \exp(\sigma kT), \quad k \in \mathbb{N},$$

where T is the period of the two-dimensional periodic base flow and $\mu \equiv \exp(\sigma T)$ is the leading multiplier, associated with the leading eigenmode $[\tilde{\mathbf{u}}_0, \tilde{p}_0]$.

Here, the base flow is not periodic but chaotic and the evolution of the perturbation field cannot be expected to be exactly modal. However, since two-dimensional chaotic vortex shedding retains a high degree of periodicity, the time evolution of the perturbation happens to be quasi-modal. Figures 20(a)–20(c) show an example of the growth of the single Fourier mode with $\beta_z = 20.94$ on top of the chaotic two-dimensional base flow. A pseudo-periodic chaotic solution as we have has no unique period so that we choose to define it as the flight time between consecutive crossings of a purposely devised Poincaré section: $T_k = t_k - t_{k-1}$. In our case, the Poincaré section is pierced by the phase map trajectory every time $C_L = 0$ and $dC_L/dt < 0$, as indicated by the dashed line and the circles in Fig. 20(a). The kinetic energy E_{β_z} contained in the unique spanwise Fourier mode employed in the simulation is shown in Fig. 20(b). After some initial transients with a slight decrease, the modal energy starts increasing, following an exponential trend for $t \gtrsim 10$ until nonlinear saturation occurs for $t \gtrsim 30$. The energy levels of the unique spanwise mode of wavenumber β_z at the Poincaré crossings are marked with circles, and the multipliers μ_k estimated at crossing k from the energy ratio between consecutive crossings $k-1$ and k as

$$\frac{E_{\beta_z}^k}{E_{\beta_z}^{k-1}} = \frac{\|\tilde{\mathbf{u}}^k\|_{L_2}^2}{\|\tilde{\mathbf{u}}^{k-1}\|_{L_2}^2} = \exp(2\sigma T_k) \equiv \mu_k^2,$$

where $\|\cdot\|_{L_2}$ denotes the L_2 norm, are plotted in Fig. 20(c). As expected for an unstable base flow, the multiplier is greater than unity, but unlike what happens for an exactly periodic base flow,

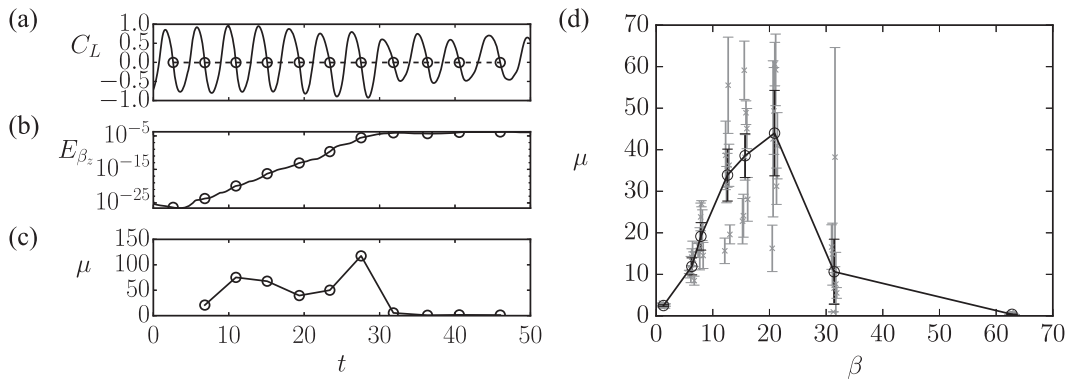


FIG. 20. Quasi-modal evolution of a perturbation with $\beta_z = 2\pi/\lambda_z = 20.94$ ($\lambda_z = 0.3$) on two-dimensional chaotic vortex shedding at $Re = 2000$. (a) Time evolution of C_L as used to define a Poincaré section (Poincaré crossing marked with circles). (b) Evolution of the perturbation field kinetic energy. (c) Evolution of the multiplier as computed for every two consecutive Poincaré crossings. (d) Value of the multiplier μ as a function of spanwise wavenumber β_z . Seven different initial conditions for the chaotic base flow result in the multiple sets of data for each β_z (gray). All seven are gathered in a unique curve (black line). Error-bars indicate the variability of the multiplier in time.

its value is variable along the evolution. In the case of our chaotic two-dimensional vortex shedding, the variability of the multiplier is rather large.

Up to seven different initial base state conditions along the two-dimensional chaotic vortex shedding evolution have been taken and tested for spanwise wavelengths in the range $\lambda_z \in [0.1, 10]$, corresponding to wavenumbers $\beta_z \in [0.628, 62.8]$. The results for the seven individual samples are shown in Fig. 20(d) as gray crosses with error-bars, which indicate the mean and standard deviation of the multiplier along the time evolution, respectively. In some cases, the fluctuation is small, corresponding with initial conditions at a stage of the time evolution where vortex-shedding is particularly well behaved. In others, the variability is huge. Averaging the probability distribution of μ across samples reduces the variability in the multiplier to some extent and produces a softer dependence of the multiplier on the wavenumber. The maximum growth of infinitesimal three-dimensional perturbations seems to occur for spanwise wavenumbers $\beta_z \approx 20.94$, which corresponds to a spanwise wavelength of $\lambda_z = 2\pi/\beta_z \approx 0.3$. This wavelength is in good agreement with

the spanwise size of the structures we observe in the wake region in fully three-dimensional turbulent simulations, particularly so in the very near-wake region at $(x, y) = (0.5, 0.5)$.

A snapshot of the fastest growing (leading) eigenmode, taken at the time of a Poincaré crossing within the linear regime, is depicted in Fig. 21(b), while Fig. 21(a) shows the instantaneous two-dimensional state at the exact same time. The spanwise vorticity (ω_z) colormap indicates that the mode is at its strongest along the braid region that connects the newly forming Kármán vortex core in the immediate vicinity of the cylinder and the preceding vortex of the same sign. The instability is local in the sense that exponential growth occurs only at a very precise location within the wake formation region and does not extend to the region where the wake is already in place and the Kármán vortex street is well developed. Infinitesimal perturbations of spanwise wavelength $\lambda_z = 2\pi/\beta_z = 0.3$ therefore exponentially grow only within the most recently generated braid at all times. There is no guarantee that the perturbation reaches nonlinear saturation unaltered and thus constitutes the origin of the three-dimensional structures observed in experiments and direct numerical simulation, but they certainly have the right spanwise size and are located in the precise flow regions where the structures thrive. This gives an indication that the structures observed in the wake at these transitional regimes might bear a strong connection with the fastest growing mode on the underlying two-dimensional base flow.

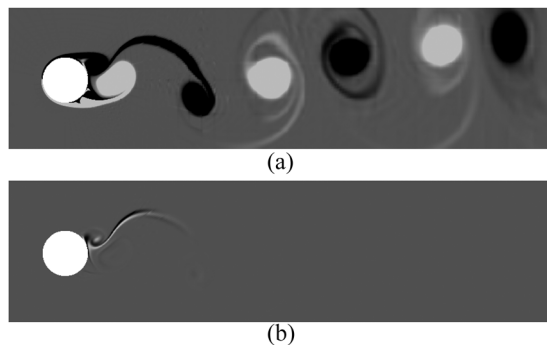


FIG. 21. Spanwise vorticity (ω_z) colormaps at the Poincaré section defined by $C_L = 0$ and $dC_L/dt < 0$ of (a) the two-dimensional chaotic vortex shedding solution ($\omega_z \in [-2, 2]$) and (b) the leading eigenmode (arbitrary symmetric ω_z range) for $\beta_z = 20.94$.

V. CONCLUSIONS

A comprehensive numerical study of the transitional flow past a circular cylinder at $Re = 2000$ has been performed in order to characterize the three-dimensional flow structures that appear in the wake. Domains smaller than $L_z < 2.5$ in the spanwise direction fail to yield correct flow statistics, possibly due to the existence of unaccounted-for large-scale motions that are precluded by a limited size.

By thoroughly analyzing flow statistics and wake topology, we settle the controversy regarding the U - vs V -shaped streamwise

velocity mean profile in the near-wake and explain the observation of one or the other as the result of taking measurements at a fixed streamwise location. Correcting the probe location according to recirculation bubble size allows recasting the same results for comparison with experiments at different Reynolds numbers. Very good agreement with literature results is thus found across a range of Reynolds numbers within the transitional regime for all sorts of flow statistics.

Sufficiently long time series have allowed for the detection of the occasional manifestation of a Kelvin–Helmholtz instability within the shear layers that originate from the detachment of the boundary layers at either side of the cylinder and flap synchronous to the generation of Kármán vortices. At $Re = 2000$, Kelvin–Helmholtz vortices have been observed from time to time, with a frequency of $f_{KH} \simeq 0.84$ that closely matches experimental observation and the trends derived from first principles and scaling/dimensional analysis. The instability appears as a broad band peak in the spectrum of any velocity signal measured in the cylinder near-wake, and the associated spanwise vortices feature a certain spanwise localization in contrast with the spanwise-independent nature of the inviscid Kelvin–Helmholtz instability of a perfectly parallel shear layer.

As a first approach to characterizing the three-dimensionality in the wake, the flow has been decomposed into a primary two-dimensional signal and a secondary signal containing the remaining three-dimensional structure. This has led to the observation that three-dimensionality occurs primarily in the braid region and attains its maximum with a phase lag of approximately $5/8$ rad with respect to the maximum of the primary flow at any given location along the wake, which corresponds to the passage of a Kármán vortex.

To further investigate the features of the three-dimensional structures that appear in the wake, the Hilbert transform of a signal along a spanwise probe array has been employed to derive instantaneous spanwise size distributions of vortical structures and phase-averaging has been conducted to analyze the evolution of the distributions along the vortex-shedding cycle. We have found that the most energetic spanwise-localized structures correspond to the passage of a braid through the probe location. The maximum occurs twice along a vortex-shedding cycle due to the arched shape of the braid, and the most probable size of the structures is found to be around $\lambda_z \simeq 0.20\text{--}0.28$ at $(x, y) = (3, 0.5)$, the smaller sizes corresponding to the leading and the larger sizes corresponding to the trailing regions of the braid, respectively. We have measured the typical structure size at different locations along the wake and found that after a fast drop in the very near wake, the sizes start growing progressively for $x > 2.5$ and asymptotically reach a maximum of $\lambda_z = 0.4$ for $\lambda_z > 20$. While the sizes are found to be significantly smaller than those reported in experimental and numerical results at $Re = 3900$, the trends are similar. No difference has been found between measurements with probes at $y = 0.5$ and $y = 1$, except that the latter does not register significant three-dimensionality for $x < 3$.

By analyzing the typical spanwise spacing among streamwise vortices, we have observed that the most frequent vortex-pair count in our $L_z = 2.5$ domain is $N_{vp}^{\max} = 0.5$ (an isolated vortex), followed closely by 1 (two vortices or a vortex pair), corresponding to most probable average spacings $l_z^{\max} \simeq 2.5$ and 1.25, respectively. This seems to indicate that our domain properly captures the spacing

distribution up to its maximum and that shorter domains would tend to artificially squeeze the three-dimensional structures into spanwise extents that would not be selected naturally in the limit of very long cylinders. We believe that this might be one of the reasons behind the failure of small spanwise domains to produce correct turbulent wake statistics, but the ultimate culprit, possibly related to the existence of large-scale motions of this length scale, remains a mystery.

To try and understand the origin of the three-dimensional structures observed in the wake, we have analyzed the growth, in the linear regime, of quasi-modal perturbations added to the underlying two-dimensional chaotic vortex-shedding flow. The fastest growing perturbations happen to be localized in the braid region that connects the last forming Kármán vortex with the immediately preceding one, and they have a spanwise wavelength of $\lambda_z \simeq 0.3$. The close coincidence in the size and location of these quasi-modal perturbations with the three-dimensional structures observed in direct numerical simulation points at a close relation. We surmise that the latter are the result of the nonlinear saturation of the former, although the interactions among the full range of unstable leading eigenmodes as well as the distance from the critical Reynolds number at which the instabilities occur in the first place render it difficult to establish a direct connection between the linear and nonlinear regimes.

ACKNOWLEDGMENTS

This work was financed by the Spanish and Catalan Governments under Grant Nos. FIS2016-77849-R and 2017-SGR-00785, respectively. The authors also thankfully acknowledge the computer resources at MareNostrum and Calendula accessed through Grant Nos. RES-FI-2017-2-0020 and RES-FI-2017-3-0009, respectively.

The authors declare no conflict of interest.

DATA AVAILABILITY

The data that support the findings of this study are available from the corresponding author upon reasonable request.

REFERENCES

- C. H. K. Williamson, "Vortex dynamics in the cylinder wake," *Annu. Rev. Fluid Mech.* **28**, 477–539 (1996).
- E. Berger and R. Wille, "Periodic flow phenomena," *Annu. Rev. Fluid Mech.* **4**(1), 313–340 (1972).
- A. V. Dovgal, V. V. Kozlov, and A. Michalke, "Laminar boundary layer separation: Instability and associated phenomena," *Prog. Aeronaut. Sci.* **30**(1), 61–94 (1994).
- R. L. Simpson, "Turbulent boundary-layer separation," *Annu. Rev. Fluid Mech.* **21**(1), 205–232 (1989).
- M. M. Rai, "A computational investigation of the instability of the detached shear layers in the wake of a circular cylinder," *J. Fluid Mech.* **659**, 375–404 (2010).
- M. Thompson, K. Hourigan, and J. Sheridan, "Three-dimensional instabilities in the wake of a circular cylinder," *Exp. Therm. Fluid Sci.* **12**(2), 190–196 (1996).
- T. von Kármán, "Über den mechanismus des widerstandes, den ein bewegter körper in einer flüssigkeit erfährt," *Nachr. Ges. Wiss. Göttingen Math.-Phys. Kl.* **1911**, 509–517.
- T. von Kármán, "Über den mechanismus des widerstandes, den ein bewegter körper in einer flüssigkeit erfährt," *Nachr. Ges. Wiss. Göttingen Math.-Phys. Kl.* **1912**, 547–556.

- ⁹R. D. Henderson, "Details of the drag curve near the onset of vortex shedding," *Phys. Fluids* **7**(9), 2102–2104 (1995).
- ¹⁰D. Barkley and R. D. Henderson, "Three-dimensional Floquet stability analysis of the wake of a circular cylinder," *J. Fluid Mech.* **322**, 215–241 (1996).
- ¹¹T. Sarpkaya, "Vortex-induced oscillations: A selective review," *J. Appl. Mech.* **46**(2), 241–258 (1979).
- ¹²N. Ferguson and G. V. Parkinson, "Surface and wake flow phenomena of the vortex-excited oscillation of a circular cylinder," *J. Eng. Ind.* **89**(4), 831–838 (1967).
- ¹³C. H. K. Williamson and R. Govardhan, "Vortex-induced vibrations," *Annu. Rev. Fluid Mech.* **36**(1), 413–455 (2004).
- ¹⁴J. C. Hardin and S. L. Lamkin, "Aeroacoustic computation of cylinder wake flow," *AIAA J.* **22**(1), 51–57 (1984).
- ¹⁵M. S. Howe, *Frontmatter*, Cambridge Monographs on Mechanics (Cambridge University Press, 1998), pp. i–vi.
- ¹⁶C. H. K. Williamson, "Mode A secondary instability in wake transition," *Phys. Fluids* **8**(6), 1680–1682 (1996).
- ¹⁷R. D. Henderson and D. Barkley, "Secondary instability in the wake of a circular cylinder," *Phys. Fluids* **8**(6), 1683–1685 (1996).
- ¹⁸C. H. K. Williamson, "The existence of two stages in the transition to three-dimensionality of a cylinder wake," *Phys. Fluids* **31**(11), 3165–3168 (1988).
- ¹⁹A. Roshko, "On the development of turbulent wakes from vortex streets," Technical Report 1191, National Advisory Committee for Aeronautics, 1954.
- ²⁰M. S. Bloor, "The transition to turbulence in the wake of a circular cylinder," *J. Fluid Mech.* **19**(2), 290–304 (1964).
- ²¹C. H. K. Williamson, "The natural and forced formation of spot-like 'vortex dislocations' in the transition of a wake," *J. Fluid Mech.* **243**, 393–441 (1992).
- ²²L. Schiller and W. Linke, "Druck- und reibungswiderstand des zylinders bei Reynoldsschen zahlen 5000 bis 40000," *Z. Flugtech. Motorluft.* **24**, 193–198 (1933).
- ²³A. Prasad and C. H. K. Williamson, "The instability of the shear layer separating from a bluff body," *J. Fluid Mech.* **333**, 375–402 (1997).
- ²⁴C. H. K. Williamson, J. Wu, and J. Sheridan, "Scaling of streamwise vortices in wakes," *Phys. Fluids* **7**(10), 2307–2309 (1995).
- ²⁵T. Wei and C. R. Smith, "Secondary vortices in the wake of circular cylinders," *J. Fluid Mech.* **169**, 513–533 (1986).
- ²⁶A. Kourta, H. C. Boisson, P. Chassaing, and H. H. Minh, "Nonlinear interaction and the transition to turbulence in the wake of a circular cylinder," *J. Fluid Mech.* **181**, 141–161 (1987).
- ²⁷C. Norberg, "Effects of Reynolds number and a low-intensity freestream turbulence on the flow around a circular cylinder," Technical Report 87/2, Chalmers University, Göteborg, Sweden, 1987.
- ²⁸A. Prasad and C. H. K. Williamson, "The instability of the separated shear layer from a bluff body," *Phys. Fluids* **8**(6), 1347–1349 (1996).
- ²⁹A. Roshko, "Perspectives on bluff body aerodynamics," *J. Wind Eng. Ind. Aerodyn.* **49**(1), 79–100 (1993).
- ³⁰S. Szepeszy and P. W. Bearman, "Aspect ratio and end plate effects on vortex shedding from a circular cylinder," *J. Fluid Mech.* **234**, 191–217 (1992).
- ³¹C. Norberg, "An experimental investigation of the flow around a circular cylinder: Influence of aspect ratio," *J. Fluid Mech.* **258**, 287–316 (1994).
- ³²C. H. K. Williamson, "Three-dimensional transition in the near wake of a cylinder," *Bull. Am. Phys. Soc.* **32**, 2098 (1987).
- ³³H. Mansy, P.-M. Yang, and D. R. Williams, "Quantitative measurements of three-dimensional structures in the wake of a circular cylinder," *J. Fluid Mech.* **270**, 277–296 (1994).
- ³⁴H. Q. Zhang, U. Fey, B. R. Noack, M. König, and H. Eckelmann, "On the transition of the cylinder wake," *Phys. Fluids* **7**(4), 779–794 (1995).
- ³⁵J. Wu, J. Sheridan, M. C. Welsh, and K. Hourigan, "Three-dimensional vortex structures in a cylinder wake," *J. Fluid Mech.* **312**, 201–222 (1996).
- ³⁶B. R. Noack and H. Eckelmann, "A global stability analysis of the steady and periodic cylinder wake," *J. Fluid Mech.* **270**, 297–330 (1994).
- ³⁷C. K. Chyu and D. Rockwell, "Near-wake structure of an oscillating cylinder: Effect of controlled shear-layer vortices," *J. Fluid Mech.* **322**, 21–49 (1996).
- ³⁸S. Gsell, R. Bourguet, and M. Braza, "Three-dimensional flow past a fixed or freely vibrating cylinder in the early turbulent regime," *Phys. Rev. Fluids* **3**, 013902 (2018).
- ³⁹I. Wygnanski, F. Champagne, and B. Marasli, "On the large-scale structures in two-dimensional, small-deficit, turbulent wakes," *J. Fluid Mech.* **168**, 31–71 (1986).
- ⁴⁰W. K. George, "Asymptotic effect of initial and upstream conditions on turbulence," *J. Fluids Eng.* **134**(6), 061203 (2012).
- ⁴¹Y. Zhou and R. Antonia, "Effect of initial conditions on characteristics of turbulent far wake," *JSME Int. J., Ser. B* **37**(4), 718–725 (1994).
- ⁴²G. L. Brown and A. Roshko, "Turbulent shear layers and wakes," *J. Turbul.* **13**, N51 (2012).
- ⁴³S. L. Tang, R. A. Antonia, L. Djenidi, and Y. Zhou, "Complete self-preservation along the axis of a circular cylinder far wake," *J. Fluid Mech.* **786**, 253–274 (2016).
- ⁴⁴Y. Zhou, R. A. Antonia, and W. K. Tsang, "The effect of Reynolds number on a turbulent far-wake," *Exp. Fluids* **25**(2), 118–125 (1998).
- ⁴⁵L. M. Lourenco and C. Shih, "Characteristics of the plane turbulent near wake of a circular cylinder, a particle image velocimetry study," Taken from Beaudan and Moin⁵⁰, 1993.
- ⁴⁶Y. Zhou and R. A. Antonia, "A study of turbulent vortices in the near wake of a cylinder," *J. Fluid Mech.* **253**, 643–661 (1993).
- ⁴⁷L. Ong and J. Wallace, "The velocity field of the turbulent very near wake of a circular cylinder," *Exp. Fluids* **20**(8), 441–453 (1996).
- ⁴⁸C. Norberg, "LDV-measurements in the near wake of a circular cylinder," ASME Paper No. FEDSM98-521, 1998.
- ⁴⁹P. Parnaudeau, J. Carlier, D. Heitz, and E. Lamballais, "Experimental and numerical studies of the flow over a circular cylinder at Reynolds number 3900," *Phys. Fluids* **20**(8), 085101 (2008).
- ⁵⁰P. Beaudan and P. Moin, "Numerical experiments on the flow past a circular cylinder at sub-critical Reynolds number," Technical report, NASA STI/Recon Technical Report No. TF-62, December 1994.
- ⁵¹R. Mittal, "Progress on LES of flow past a circular cylinder," Technical Report CA 9430, Center for Turbulence Research, 1996.
- ⁵²M. Breuer, "Large eddy simulation of the subcritical flow past a circular cylinder: Numerical and modeling aspects," *Int. J. Numer. Methods Fluids* **28**(9), 1281–1302 (1998).
- ⁵³X. Ma, G.-S. Karamanos, and G. E. Karniadakis, "Dynamics and low-dimensionality of a turbulent near wake," *J. Fluid Mech.* **410**, 29–65 (2000).
- ⁵⁴A. G. Kravchenko and P. Moin, "Numerical studies of flow over a circular cylinder at $Re_D = 3900$," *Phys. Fluids* **12**(2), 403–417 (2000).
- ⁵⁵J. Franke and W. Frank, "Large eddy simulation of the flow past a circular cylinder at $Re = 3900$," *J. Wind Eng. Ind. Aerodyn.* **90**(10), 1191–1206 (2002).
- ⁵⁶O. Lehmkuhl, I. Rodríguez, R. Borrell, and A. Oliva, "Low-frequency unsteadiness in the vortex formation region of a circular cylinder," *Phys. Fluids* **25**(8), 085109 (2013).
- ⁵⁷C. Norberg, "Fluctuating lift on a circular cylinder: Review and new measurements," *J. Fluids Struct.* **17**(1), 57–96 (2003).
- ⁵⁸E. Konstantinidis, S. Balabani, and M. Yianneskis, "The effect of flow perturbations on the near wake characteristics of a circular cylinder," *J. Fluids Struct.* **18**(3-4), 367–386 (2003).
- ⁵⁹E. Konstantinidis, S. Balabani, and M. Yianneskis, "Conditional averaging of PIV plane wake data using a cross-correlation approach," *Exp. Fluids* **39**(1), 38–47 (2005).
- ⁶⁰E. Konstantinidis and S. Balabani, "Flow structure in the locked-on wake of a circular cylinder in pulsating flow: Effect of forcing amplitude," *Int. J. Heat Fluid Flow* **29**(6), 1567–1576 (2008).
- ⁶¹S. Dong, G. E. Karniadakis, A. Ekmekci, and D. Rockwell, "A combined direct numerical simulation-particle image velocimetry study of the turbulent near wake," *J. Fluid Mech.* **569**, 185–207 (2006).
- ⁶²H. Ouvrard, B. Koobus, A. Dervieux, and M. V. Salvetti, "Classical and variational multiscale LES of the flow around a circular cylinder on unstructured grids," *Comput. Fluids* **39**(7), 1083–1094 (2010).

- ⁶³I. Afgan, Y. Kahil, S. Benhamadouche, and P. Sagaut, "Large eddy simulation of the flow around single and two side-by-side cylinders at subcritical Reynolds numbers," *Phys. Fluids* **23**(7), 075101 (2011).
- ⁶⁴H. Chen, Z. Li, and Y. Zhang, "U or V shape: Dissipation effects on cylinder flow implicit large-eddy simulation," *AIAA J.* **55**(2), 459–473 (2016).
- ⁶⁵F. Tremblay, "Direct and large-eddy simulation of flow around a circular cylinder at subcritical Reynolds numbers," Ph.D. thesis, Technische Universität München, 2002.
- ⁶⁶R. Mittal, "Large-eddy simulation of flow past a circular cylinder," in *Annual Research Briefs 1995* (Center for Turbulence Research, 1995), pp. 107–116.
- ⁶⁷A. H. Mohammad, Z. J. Wang, and C. Liang, "Large eddy simulation of flow over a cylinder using high-order spectral difference method," *Adv. Appl. Math. Mech.* **2**(4), 451–466 (2010).
- ⁶⁸G. Lodato and A. Jameson, "LES modeling with high-order flux reconstruction and spectral difference schemes," in *ICCFD7 Conference 2012* (Citeseer, 2012), Vol. 2201, pp. 9–13.
- ⁶⁹J. G. Wissink and W. Rodi, "Numerical study of the near wake of a circular cylinder," *Int. J. Heat Fluid Flow* **29**(4), 1060–1070 (2008).
- ⁷⁰R. D. Peltzer, "The effect of upstream shear and surface roughness on the vortex shedding patterns and pressure distributions around a circular in transitional Reynolds number flows," M.Sc. thesis, VPI and SU, 1980, <https://ci.nii.ac.jp/naid/10010461630/en/>.
- ⁷¹H. G.-C. Woo, J. A. Peterka, and J. E. Cermak, "Experiments on vortex shedding from stationary and oscillating cables in a linear shear flow," Technical Report CER; 81/82-7, Colorado State University, Libraries, 1981.
- ⁷²J. H. Gerrard, "Experimental investigation of separated boundary layer undergoing transition to turbulence," *Phys. Fluids* **10**(9P2), S98 (1967).
- ⁷³A. Prasad and C. H. K. Williamson, "Three-dimensional effects in turbulent bluff-body wakes," *J. Fluid Mech.* **343**, 235–265 (1997).
- ⁷⁴C. D. Cantwell, D. Moxey, A. Comerford, A. Bolis, G. Rocco, G. Mengaldo, D. De Grazia, S. Yakovlev, J.-E. Lombard, D. Ekelschot, B. Jordi, H. Xu, Y. Mohamied, C. Eskilsson, B. Nelson, P. Vos, C. Biotto, R. M. Kirby, and S. J. Sherwin, "Nektar++: An open-source spectral/hp element framework," *Comput. Phys. Commun.* **192**, 205–219 (2015).
- ⁷⁵C. H. K. Williamson, "Three-dimensional wake transition," *J. Fluid Mech.* **328**, 345–407 (1996).